universität wien

MASTERARBEIT / MASTER'S THESIS

Titel der Masterarbeit / Title of the Master's Thesis

„Mechanisms of hardening in biodegradable Mg and Mg–Alloys through different thermal and mechanical processing routes“

verfasst von / submitted by

Katharina Werbach, BSc

angestrebter akademischer Grad / in partial fulfilment of the requirements for the degree of

Master Of Science (MSc)

Wien, 2016 / Vienna, 2016

Studienkennzahl lt. Studienblatt / degree programme code as it appears on the student record sheet:	A 066 876
Studienrichtung lt. Studienblatt / degree programme as it appears on the student record sheet:	Masterstudium Physik UG2002
Betreut von / Supervisor:	ao. Univ.-Prof. Dr. Michael Zehetbauer

Danksagung:

Ich möchte mich zuallererst an dieser Stelle bei all denjenigen bedanken, die mich während der Anfertigung dieser Master-Arbeit untersttzt und motiviert haben.
In erster Linie möchte ich dabei meinem Betreuer, ao. Univ.-Prof. Dr. Michael Zehetbauer, für die Hilfe bei der Themenfindung, die intensive Betreuung und der Möglichkeit an einem internationalen Projekt mitzuarbeiten danken. Auch den nachfolgenden Personen, sowie meinen Kollegen und Kolleginnen der Gruppe "Physik Nanostrukturierter Materialien", gilt mein besonderer Dank. Sie alle haben maßgeblich daran mitgewirkt, dass diese Arbeit nun in dieser Form vorliegt.

- Mag. Dr. Jelena Horky
- Prof. Jörg F. Löffler
- Mag. Dr. Clemens Nagel
- Mag. Dr. Stephan Puchegger
- Martina Rohrer
- ao. Univ.-Prof. Mag. Dr. Erhard Schafler
- Robin Schublin
- Ao. Univ.-Prof. Mag. Dr. Bogdan Sepiol
- Prof. Peter J. Uggowitzer

Ebenso bedanke ich mich bei meinen Eltern, ohne deren Geduld und Unterstützung ich mein Studium kaum hätte beenden können.

Kurzfassung

Mg–Materialien verschiedener Reinheitsgrade sowie Mg legiert mit Zn und Ca wurden verschiedenen thermischen und mechanischen Behandlungen unterworfen. Anschließend wurde ihre Festigkeit mittels Meßung der Vickers Mikrohärte (HV) bestimmt.

Die Proben wurden entweder abgeschreckt oder mittels Hochdrucktorsion (HPT) verformt und daraufhin im Temperaturbereich zwischen 50°C–200°C gealtert.

Sowohl die abgeschreckten als auch die HPT–verformten Proben jedes Materials zeigten einen deutlichen Anstieg der HV nach dem Altern, der auch größer als der in ausschließlich verformten bzw. abgeschreckten Proben war. In allen untersuchten Materialien war ein HVMaximum im Temperaturbereich zwischen 90°C-150°C zu beobachten, während Behandlungen bei höheren Temperaturen zu einer Abnahme der Härte führten. Nur die HV von schwach verformten Proben zeigte eine sofortige Abnahme nach dem Altern. Um die Ursachen für den Anstieg der HV zu untersuchen wurden reines Mg und Mg-Zn-Ca mit elektronenmikroskopischen Methoden untersucht. In Mg-Zn-Ca Proben konnten dabei für alle Behandlungen- abgeschreckt, verformt mit und ohne anschließendes Altern- große Ca-Oxid Partikel nachgewiesen werden, während die HPT-verformte und auch die anschließend gealterte Probe auch kleine Ca-reiche Ausscheidungen aufwies. Die Dichte dieser Ausscheidungen stieg zwar während des Alterns an, jedoch in einem viel zu geringem Ausmaß, als das der Anstieg der HV dadurch allein erklärt werden konnte.

Kleine Versetzungringe konnten in HPT verformten Proben aus reinem Mg nachgewiesen werden; in anschließend gealterten Proben waren auch größere Versetzungsringe zu beobachten.

Zusammenfassend wird daher vorgeschlagen, den beobachteten Härtungseffekt auf Bildung und Wachstum von aus Leerstellen gebildeten Versetzungsrigen bzw. der Bildung von Leerstellenagglomeraten zurckzufhren. Diese Defekte bilden sich möglicherweise während des Abschreckens bzw. der Verformung, sicherlich aber während des darauffolgenden Alterns .

Abstract

Mg materials of different purities, as well as Mg–alloys containing Zn and Ca have been processed by different thermal and mechanical treatments, and their strength was continuously investigated by Vickers microhardness (HV) measurements. The treatment consisted of either quenching or of High Pressure Torsion–deformation (HPT) and of subsequent aging at temperatures between 50°C – 200°C.

During aging, both the quenched and HPT deformed specimens of all types of materials showed a marked increase of HV which was larger than that found in solely quenched or HPT-processed specimens. In all investigated materials a maximum of HV occurred at aging temperatures between 90° – 150°C followed by a decrease of HV at higher aging temperatures; only the HV of weakly deformed specimens immediately decreased during aging. To find out the reasons for the maximum in HV, several methods of Electron Microscopy have been applied on two materials, pure Mg and a Mg-Zn-Ca alloy. Samples out of the Mg-Zn-Ca alloy being quenched and aged, or HPT deformed, or HPT deformed and aged showed large Calcium Oxide particles in every specimen, as well as small Ca-rich precipitations in the HPT deformed and additionally aged specimens. Although the density of these precipitations increased with aging, quantitative estimations of precipitation hardening showed that the latter could by far not account for the marked increase in HV. Samples out of pure Mg showed small dislocation loops in HPT-deformed and larger dislocation loops in additionally aged specimens.

In conclusion it is proposed that the observed hardening effect is caused by the formation and coarsening of vacancy-type dislocation loops and/or agglomerates which may develop already during quenching or during HPT deformation, but certainly during thermal aging.

Contents

Chapter 1

Introduction

1.1 Biodegradable Magnesium Implants

Magnesium, with the atomic number 12, is a light metal and a common metal in the earth crust. Its pure form was synthesized first by Antoine Bussy in 1828 and nowadays is a common and popular material in construction, agriculture and medicine [1]. Its advantages as an industrially used metal include the lowest density of all metallic constructional materials and a high specific strength, but it also has a low elastic modulus and high chemical reactivity [2].
Those last two points – which impede the industrial use of Magnesium – make it a very attractive candidate for the use as biodegradable implant. It has been considered for such a purpose for almost 150 years, with various areas of application [3]. The use as an osteosynthetic material in particular was presumably suggested first by Payr in 1900, who put the use of pins, nails, wires, pegs, sheets and plates made of Magnesium forward ([4][3][5]).
Compared to commonly used implant– and fixture–materials the mechanical properties of Magnesium are more compatible to the bone [6], which makes it an attractive candidate for such purposes.

	Bone	Mg	Titanium Alloy
Elastic Modulus [GPa]	17-20 [7]	41-45 [1]	110-117[6]
-Yield Strength [MPa]	77-95 [7]	21-150 [1]	380-875 [8]

Table 1.1: Mechanical properties of the human femoral bone, Magnesium and Titanium alloys

Although successful treatments of patients were reported by Payr and contemporary authors, until now Magnesium implants don't play an important role in surgery [3]. It has been speculated that the reason lies in the unpredictable corrosion of Magnesium and the subsequent loss of mechanical support [5].
Furthermore, Magnesium – as a soft and brittle metal – is of limited suitability for

load–bearing purposes, which should be guaranteed during degradation. Alloying Magnesium with other metals to influence degradation properties has been discussed since the beginning [3], but simultaneously optimizing the mechanical properties remains a challenge.

1.2 Previous Works

In a recent work by Horky et al. ([9],[10]) the Vickers hardness HV of a biodegradable Magnesium–Zinc–Calcium alloy, which previously was processed by High Pressure Torsion (HPT, see chapter 3.2.3 for a detailed explanation) and subsequently aged, was investigated. The samples were either not deformed or HPT–processed at 4 GPa by either 2 rotations (corresponding to $\gamma \approx 31$, see 3.2.3) or 0,15 rotations (corresponding to $\gamma \approx 2$) and afterward aged in a silicon oil bath for one hour. The results of the HV measurements are shown in figure 1.1 below. A strong increase in HV after aging can be observed in samples HPT–processed by $\gamma \approx 31$, while samples HPT–processed by $\gamma \approx 2$ show a less pronounced increase and the non deformed samples no significant change in HV at all.

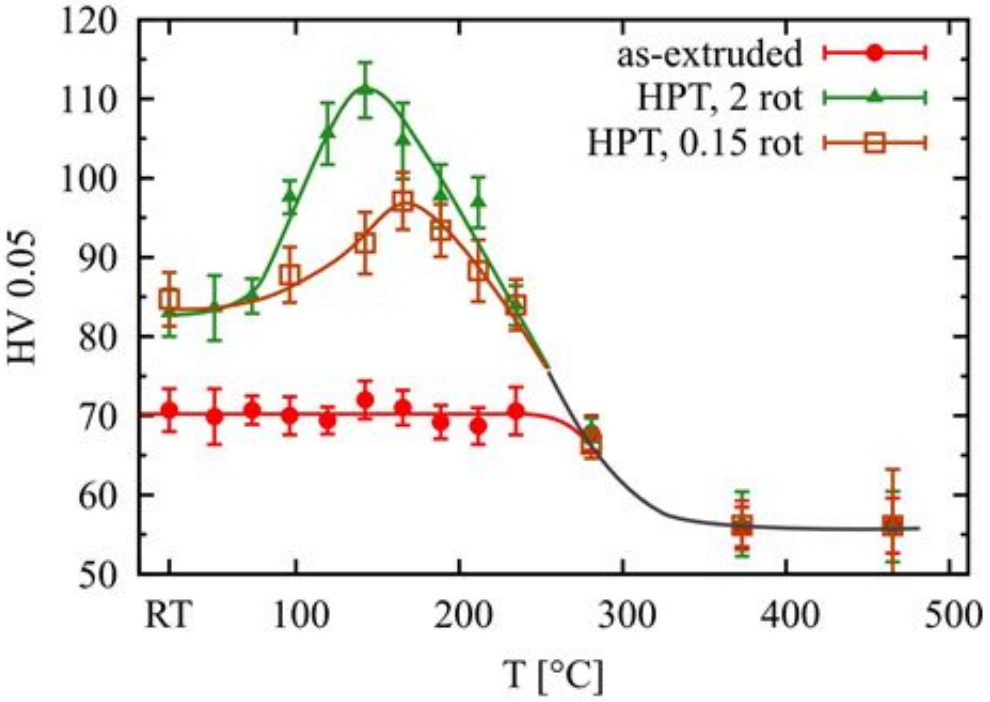

Figure 1.1: HV of a HPT–processed and aged Mg–Zn–Ca alloy ([9],[10]), courtesy of the authors

A likely explanation for this behavior in the case at hand would be the precipitation of Calcium–rich particles during aging, which would lead to an increase in hardness via precipitation–hardening. Further investigations with transmission

electron microscopy (TEM), scanning electron microscopy (SEM) and atom probe tomography (APT) were carried out with the result that not only the grain size does not change, but also no new Ca–rich particles precipitate during aging [1]([9],[10]).
While an increase in hardness or strength after aging of plastically deformed metals is an unusual effect, the increase of strength after aging quenched samples from temperatures near the melting point is well known as "Quench Hardening". This particular effect can be traced back to the agglomeration of vacancies – which exist in supersaturation after quenching – to large vacancy clusters or loops and has been studied extensively in the past (see for example [11] [12]).
The case of Magnesium in particular was investigated in 1974 in an article by Hampshire and Hardie [13], where an increase in flow stress up to 60% could be achieved via quenching and subsequent aging of polycrystalline Magnesium of 99.95% purity (commercially pure Magnesium, abbreviated "CP–Mg"). Specimens were quenched from 525°C and subsequently aged for different lengths of time at temperatures between 25°C and 330°C. Afterward, tensile tests were performed and the 0,1% flow stress was measured. Figure 1.2 shows the effects of 10 min isochronal aging on the flow stress increment of from 525°C quenched samples.

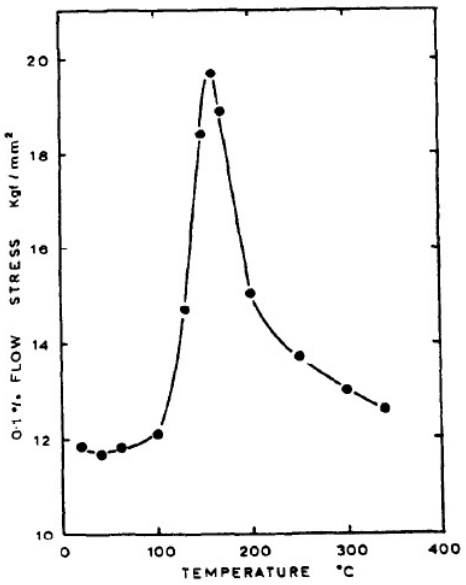

Figure 1.2: Increase of the 0,1% flow stress with aging temperature after quenching [13]

The authors suggest that this increase might be due to the formation of prismatic loops in the course of aging of the quenched specimens and provide TEM images of not only prismatic loops but also other complex defect structures (see figure 1.3 below).

They also made a first attempt of modeling the effect, starting with Orowan's

[1] although μm-sized Ca-rich precipitations could be found in all samples in equal density

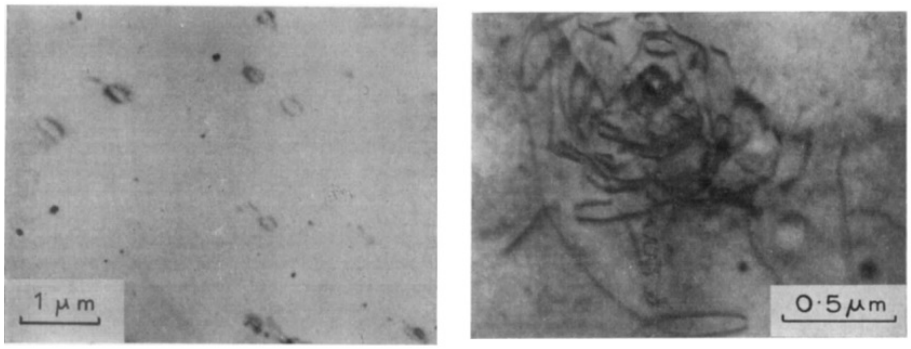

Figure 1.3: Loops in quenched/aged CP–Mg (left) and other complex dislocation structures in purely quenched CP–Mg (right). [13]

equation (see chapter 2.2.3) and proposed equation 1.1 (below) to describe the dependence of the strength increment $\Delta\sigma$ on the material parameters G (shear modulus) and b (Burgers vector) as well as the number of loops N and their diameter d.

$$\Delta\sigma = \frac{Gb}{k}\,(Nd)^{1/2} \tag{1.1}$$

The results of Hampshire and Hardie have been evaluated further by Kirchner [14], whose results will be discussed in chapter 2.2.3.
The generation of vacancies during plastic deformation is a well known effect [12] and has been observed in the past in high concentrations in SPD–processed metals ([15] [16]).

1.3 Aim of this Work

The similarity of the effects observed by Hampshire and Hardie [13] and Horky et al. ([9],[10]) leads to the hypothesis that the coarsening or even the formation of prismatic loops and vacancy clusters takes place during aging after SPD–processing and leads to a significant hardening.
This work aims to investigate the above mentioned hypothesis by comparing the results reported by Horky et al. ([9],[10]) to data gained by quenching and subsequent aging of the same Mg–Zn–Ca alloy. Furthermore, a Magnesium–Zinc alloy and pure Magnesium will be will be studied with respect to their Vickers hardness after quenching/aging to determine the role alloying elements play in quench hardening of Magnesium. The results of Horky et al. ([9],[10]) will also be compared to the results gained by similarly processing commercially pure and ultra–high pure Magnesium (see chapter 3.1.1) to determine the role alloying elements play in the HPT–processing of Magnesium.

Chapter 2

Theoretical Background: The Strength of Hexagonal Metals

The *Springer Handbook of Materials Measurement Methods* defines hardness "as the resistance of a material to permanent penetration by another material"([17]311). A hardness measurement is performed by testing the resistance of a test block with an indenter of specified shape and material. The result is, therefore, always dependent on the way the measurement is performed, especially by the material and shape of the indenter, and various standardized procedures have been established in the past to ensure comparability of the results([17] 313). As the parameter "hardness" always stems from plastic deformation, the chapters 2.1 and 2.2 provide an overview of plastic deformation in materials with hexagonal structure.

2.1 The Hexagonal Structure and Defects Therein

The hexagonal structure of materials is one of two ways to achieve a most dense arrangement of atoms (close–packed structure), the other being the face centered cubic (fcc) one. While both have the same packing efficiency of $\approx 74\%$, they differ in the arrangement of atoms (which may be assumed as solid spheres for all practical purposes). In the fcc structure every third layer of atoms directly overlaps, leading to a stacking order of ABCABCABC..., whereas in the hexagonal structure every second layer of atoms overlaps, leading to a stacking order of ABABABABAB. The close–packed plane of the hexagonal structure is the basal plane (0001) and the shortest lattice vectors are of the type $\frac{1}{3}\langle 11\bar{2}0\rangle$

2.1.1 Stacking Faults

....in the basal plane [1] are divided into three different types, the two intrinsic $\mathbf{I_1}$ and $\mathbf{I_2}$ and one extrinsic **E**. Table 2.1 (below) gives an overview of the different stacking faults and their associated energies; main contributions arise from second–neighbor sequences of the planes [12].

Typet	Reaction					Energy
$\mathbf{I_1}$	ABABABAB...	$\rightarrow$	ABA**BB**ABA....	$\rightarrow$	ABAB**CBC**B...	γ_{I1}
$\mathbf{I_2}$	ABABABAB...	$\rightarrow$	AB**CAC**ABAB...			$\gamma_{I2} \approx 2\gamma_{I1}$
E	ABABABAB...	$\rightarrow$	ABAB**C**ABAB...			$\gamma_E \approx 3\gamma_{I1}$

Table 2.1: Stacking faults of the basal plane in the hexagonal structure and their energies (after [12]p104)

2.1.2 Slip

.....in hexagonal metals can be divided into basal and non–basal slip. Since the basal plane is the close-packed one, it can be expected that the main slip system consists of the basal plane in the direction of the shortest lattice vector $\frac{1}{3}\langle 11\bar{2}0\rangle$ [12]. Other slip systems are the prismatic and pyramidal one, of the planes $\left(10\bar{1}0\right)$ and $\left(10\bar{1}1\right)$, respectively, in the same direction ([12],[18]). These are expected to have a higher critical resolved shear stress (CRSS) than the basal slip system. However, this holds only true for an ideal hexagonal structure, defined by a ratio of the cell parameters $\frac{c}{a} = \sqrt{\frac{8}{3}} \approx 1,633$, in which the basal plane is the close–packed one.
Magnesium has a $\frac{c}{a}$ ratio of 1,623 and indeed a CRSS of 0,52 MPa to 0,81 MPa [19] for the basal slip system can be observed, whereas the CRSS of the other observed slip system, the prismatic one $\left\{10\bar{1}0\right\}\frac{1}{3}\langle 11\bar{2}0\rangle$, is given with 39MPa to 52MPa [19].

2.1.3 Vacancies and Dislocation Loops

Two types of dislocation loops are observed in metals: *shear loops* whose Burgers vector $\vec{b}$ lies in the plane of the loop and *prismatic loops* whose Burgers vector points out of the dislocation plane. While the first can expand and shrink via glide (i.e. conservative motion), the latter can only expand and shrink while absorbing or emitting vacancies (or interstitial atoms) [12]. In table 2.2 the two types of dislocation loops are compared.

Vacancies in hexagonal metals can precipitate in the close–packed planes (in the ideal case, the (0001) plane) as platelets to form prismatic dislocation loops if

[1] according to Hull and Bacon [12] it is a matter of speculation whether stacking faults in other planes exist or not

	Shear loops	Prismatic loops
$\vec{b}$	in plane	out of plane
Glide plane	plane of the loop	loop glides along the dislocation line in direction of $\vec{b}$
Origin	• collapse of vacancy voids associated with formation of **E** • Orowan mechanism	• collapse of vacancy voids associated with formation of $\mathbf{I_1}$ • annihilation of dislocation dipoles • intermediate jogs • Hirsch mechanism

Table 2.2: Comparison of dislocation loops in metals, [12]

present in a higher than equilibrium concentration [12]. A list of origins is given below:

1. **Thermal Vacancies**
   Some vacancies are always present in metals due to thermal fluctuations, since there always is the chance that single atoms "escape" the crystal and leave a vacancy behind (provided the material's temperature is higher than 0°K).The atomic concentration of n such vacancies in thermal equilibrium at a temperature T in a crystal consisting of N atoms is dependent on the vacancy's enthalpy of formation G_F^V and given in equation 2.1 below [20].

$$c_V \equiv \frac{n}{N} = e^{\left(-\frac{G_F^V}{k_B T}\right)} \tag{2.1}$$

2. **Irradiation Vacancies**
   Irradiation of metals with elemental particles (e.g.: electrons, protons, neutrons, heavy ions) can also be the the cause for the formation of vacancies and point defects in general [20].

3. **Plastic deformation**
   Vacancy jogs are parts of a screw dislocation that have edge-character with a Burgers vector different from the Burgers vector of the original dislocation. Thus a jogged screw dislocation can only move non–conservatively, which requires a sufficiently high stress and thermal activation. If these conditions are satisfied the moving dislocation will leave a trail of vacancies behind [12] [2].

[2] alternatively, a trail of interstitial atoms will be left behind

2.2 Strength Effects

To increase the hardness of a material always means to hinder the glide of dislocations. In the following, three ways to harden materials will be described.

2.2.1 Grain–Boundary Hardening

Grain–boundaries impede dislocation and therefore changing the grain size leads to an increase in yield strength. This effect is described by the Hall–Petch equation (equation 2.2 below) which relates the increase in yield strength $\Delta\sigma_y^{HP}$ to the (average) grain diameter d and the material's constant k_x [21].

$$\Delta\sigma_y^{HP} = \frac{k_x}{\sqrt{d}} \tag{2.2}$$

2.2.2 Work Hardening

Because of the displacement of the atoms from their ideal positions, dislocations produce a stress field in the matrix surrounding them. The stress fields of many dislocations will interact and can impede the movement of dislocations in the crystal. Also, jogs in dislocations –formed when two dislocations cross– hinder dislocation motion trough pinning.
This causes an increase in yield strength $\Delta\sigma_y^{\rho}$ which is proportional to the dislocation density ρ, the shear modulus G and the Burgers vector$b$ and given in equation 2.3 below [20].

$$\Delta\sigma_y^{\rho} = Gb\sqrt{\rho} \tag{2.3}$$

2.2.3 Precipitation Hardening

Impenetrable, incoherent particles provide effective obstacles [12] impeding the glide of a dislocation. The parts of the dislocation close to the obstacles get pinned by them, forcing the dislocation to bow out. Orowan related this mechanism to the applied stress and proposed the well-known Orowan equation (equation 2.4 below), that relates the increase in stress τ_{OR} caused by foreign particles to the shear modulus G and the Burgers vector$b$ of the material.

$$\tau_{OR} = \frac{Gb}{l} \tag{2.4}$$

where l denotes the mean distance between precipitations in the glide-plane. Increasing the number of such obstacles – for example by precipitations of a second phase – in materials is, therefore, a way to harden them.

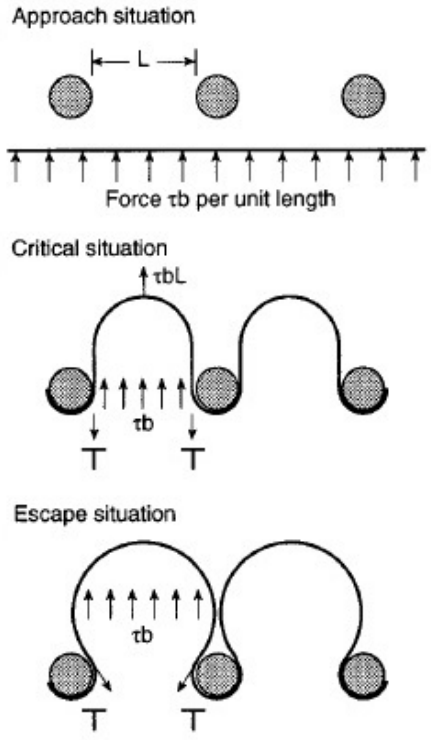

Figure 2.1: Illustration of the steps of the Orowan effect, according to [22]

Equation 2.4 has the drawback of requiring the distance between single particles in a single grain, which in practice is not an easily obtainable value. Thus, it was improved in the past, especially to consider effects of statistically distributed particles via their volume fraction f and diameter D , of polycrystallinity and the conversion from shear stress τ to tensile stress $\Delta\sigma_y$ ([22] ,[23]).

$$\Delta\sigma_y = 0,538\frac{Gb\sqrt{f}}{D}ln\left(\frac{D}{2b}\right) \tag{2.5}$$

Although impenetrable obstacles as origins of the Orowan effect are usually associated with particles of a second phase, prismatic dislocations loops haven been considered in an article by Hampshire and Hardie [13] to act as part of an "Orowan type process". They [13] could achieve an increase in flow stress of polycrystalline Magnesium up to 60% via quenching and subsequent aging which they attribute to the formation prismatic dislocation loops in the basal plane.
Especially for hexagonal metals such an effect can play an important role in increasing strength, because vacancies precipitate in the basal plane which also is part of the preferred slip system.
Kirchner [14] thoroughly investigated the data reported by Hampshire and Hardie

[13] and proposed the relationship given in equation 2.6 (below) to describe the increase in flow stress $\Delta\sigma_L$ dependent on the loop density N and their average diameter d and "some dimensionless constant" k.

$$\Delta\sigma_L = \frac{Gb}{k} N^a d^{3a-1} \tag{2.6}$$

A re-evaluation of the data provided by Hampshire and Hardie [13] in the form of plotting the increase in flow stress dependent on the loop distance – which shows a distinct division in two regions– is shown. Region I, with a low density of obstacles, is attributed to an Orowan type process, where gliding dislocations have to overcome the loops as obstacles. In region II, with a high density of loops, the dislocations have to directly overcome the high internal stress field by externally applied stress.

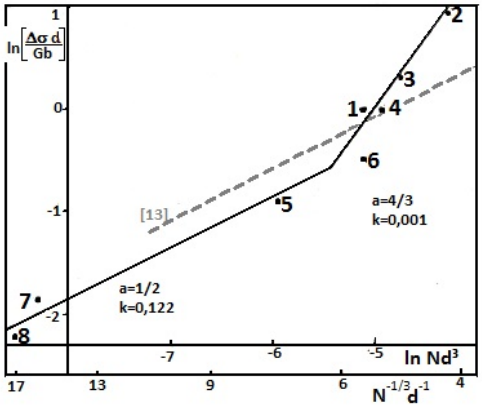

Figure 2.2: The effect of prismatic dislocation loops on strength according to Kirchner [14]

Chapter 3

Materials and Their Preparation

3.1 Investigated Materials

3.1.1 Magnesium

Pure Magnesium is a lightweight metal with a hexagonal structure. An overview about its basic physical properties is given in table 3.1.

For this work, Magnesium of two different types of purity was used:

Parameter	Value	Source
Atomic Number	12	
Density ($_{20°C}$)	1738 kgm^{-3}	[1]
Melting Temperature	650°C	[1]
Lattice Parameter ($_{20°C}$)	a=0,32092 nm ; c/a= 1,624	[1]
Elastic Modulus E ($_{polycrystalline}$)	45 GPa	[1]
Shear Modulus G ($_{polycrystalline}$)	17,3 GPa	[22]
Yield Strength YS ($_{depending\ on\ casting}$)	21-150 MPa	[1]
Burgers vector	0,321 nm	[22]

Table 3.1: Properties of Magnesium

- Commercially pure or 99.95% pure Magnesium (henceforth referred to as *CP–Magnesium* or, abbreviated, *CP–Mg*), ordered from *AlfaAesar* as slugs with a diameter of 6,35 mm (0,25 in) and a length of 12,7 mm (0,50 in).
- 99.9999 % pure Magnesium [24] (henceforth referred to as *XHP–Magnesium* or, abbreviated, *XHP–Mg*), kindly provided by Prof. P. Uggowitzer, Metal Physics and Technology, ETH-Hoenggerberg as a rod with a diameter of 6 mm.

3.1.2 The Magnesium–Zinc System

Zinc is an important commonly used alloying metal with magnesium, although it is rarely added as major alloying element [1]. It is soluble in Magnesium with 6,2wt% solubility at the first eutectic point in the phase diagram shown in figure 3.1. It also has been proposed that the binding of a Zinc impurity with a vacancy in Magnesium is energetically favorable, with a computed vacancy–binding energy of 0.05 eV for the next-neighbors [25]. For concentrations up to 5wt% Zinc also accelerates corrosion rate mildly up to ≈ 8mm/y ([1] [26]).
For this work, XHP-Magnesium alloyed with 0.3wt% Zinc (henceforth referred to as *Magnesium-Zinc* or, abbreviated,*Mg–Zn*) was kindly provided by the Health&Environment Department of the AIT Austrian Institute of Technology GmbH, Biomedical Systems. For an addition of 0.3wt% (corresponding to a mole fraction of ≈ 0,0011) Zinc, no formation of intermetallic phases is expected.

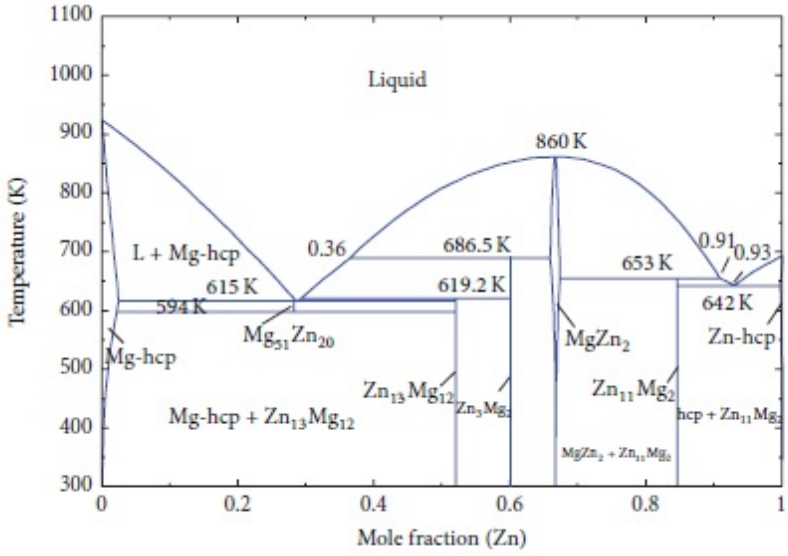

Figure 3.1: Phase Diagram of Mg-Zn System [27] [28]

3.1.3 The Magnesium–Zinc–Calcium System

Magnesium is typically alloyed with Calcium in the range of 0.01 to 3wt% to improve creep resistance [1]. For concentrations up to 5wt% it also accelerates corrosion rate moderately up to ≈ 15mm/y ([1] [26]). The phase diagram in figure 3.2 gives an overview about the solubility and intermetallic phases formed by Magnesium and Calcium. The binding of a Calcium impurity with a vacancy in Magnesium is energetically favorable and computed to be 0.06 eV for the next-neighbors [25].

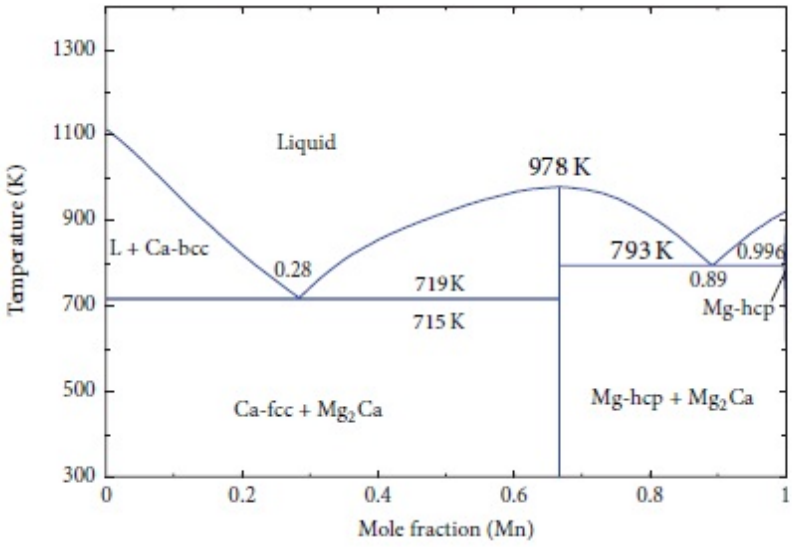

Figure 3.2: Phase Diagram of Mg-Ca System [27] [30]

Figure 3.3 shows the phase diagram of the Zinc-Calcium system. It displays eight intermediate compounds, with pronounced maxima in the liquidus line at Zinc-rich concentrations [29].

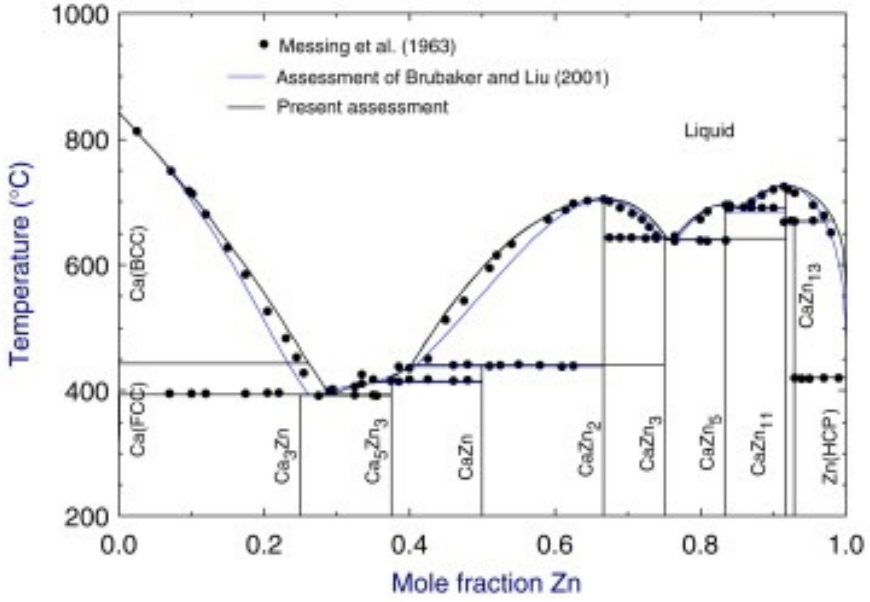

Figure 3.3: Phase Diagram of Zn-Ca System [29]

Magnesium–Zinc–Calcium alloys are relevant in the field of biodegradable metals because of the biocompatibility of each component. The alloying elements can also have an influence on corrosion and mechanical behavior:
Ternary Magnesium–Zinc–Calcium alloys with a high Zinc content are prone to form the intermatellic phase $Mg_6Zn_3Ca_2$, which acts as a cathodic site in the Magnesium matrix. In contrast, such alloys with a low Zinc content a more prone to form the

intermatellic phase $(Mg, Zn)_2Ca$, which is less noble than the Magnesium matrix and can ac as anodic site [31]. Investigations of the influence these phases have on the mechanical behavior show that $Mg_6Zn_3Ca_2$ leads to strengthening of the material, while Mg_2Ca appears to have no such effect [32].
For this work, XHP-Magnesium alloyed with 0.2wt% Zinc and 0.5wt% Calcium (henceforth referred to as *Magnesium–Zinc–Calcium* or, abbreviated, *Mg–Zn–Ca*) was used, kindly provided by LKR Leichtmetallkompetenzzentrum Ranshofen GmbH as an extruded rod with a diameter of 6 mm.

3.2 Methods of specimen preparation

3.2.1 Cutting of the Samples

All samples were brought into the appropriate shapes with a spark erosion machine. For the quenching procedure and HPT–processing (see the following sections) the material was either cut – if received as slug of an appropriate diameter – in $0,75$mm thick disks, or first cut in slices and then punched into smaller disks with a diameter of approximately 6mm.

3.2.2 Quenching

Before quenching every specimen was ground with Silicon–Carbide SiC_4 abrasive paper to remove dirt and achieve a smooth surface and thus hinder oxidation during heating. Afterward, the specimens were cleaned first with water and then isopropanol and held in place with Nickel wire on a sample holder constructed from steel foil and affixed to a long, thin Nickel rod. In each experiment two specimens were quenched simultaneously.
The set–up to quench samples (see figure 3.4) consisted of a long glass tube, which at one end was connected to a bottle of Argon, while the other end could be dipped in water. Around the middle a heating coil controlled with a *Eurotherm 2416 PID Controller* was positioned.

The sample holder was then inserted in the quenching set–up at a position in between the heating coil and the water and the current trough the heating coil as well as the Argon flow was turned on. The tip of the glass tube was dipped into a bowl filled with room–temperature water and the tube was continuously flushed with Argon for at least 20 minutes to create an oxygen-free atmosphere. After this period the samples were pushed into the heated parts of the glass tube and annealed at 550°C (while constantly flushing the tube with Argon). The samples were quenched after for one hour by manually pulling the sample holder into the water and then aged for 10 minutes at a given temperature in a silicon oil-bath and again quenched

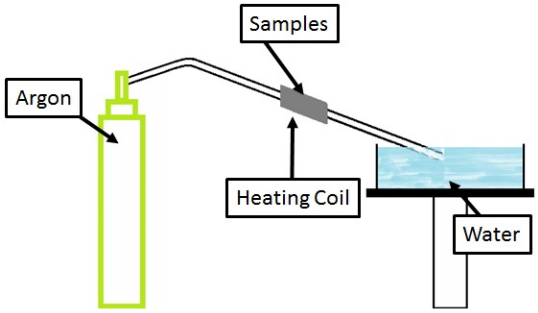

(a) Schematic design of the set–up used to quench samples

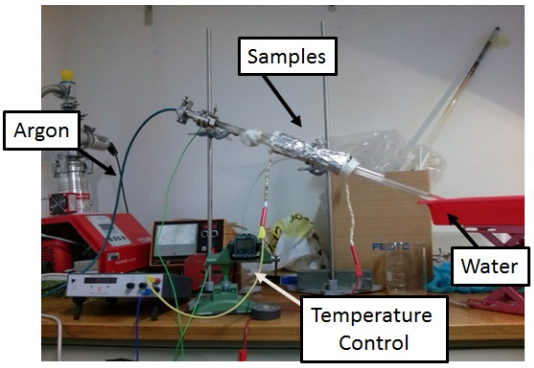

(b) The set-up used to quench samples

Figure 3.4: Quenching

in iced water.
Finally the samples ere glued to a polishing mushroom with *UHU ALLESKLEBER SUPER Strong & Safe* and ground and polished (see 3.2.5).

3.2.3 High–Pressure Torsion Deformation

High-pressure torsion (HPT) is a "top-down" procedure to obtain bulk ultrafine-grained (UFG) materials via severe plastic deformation (SPD) [33]. SPD may be defined "as any method of metal forming under extensive hydrostatic pressure that may be used to impart a very high strain to a bulk solid without the introduction of any significant change in the overall dimensions of the sample and having the ability to produce exceptional grain refinement "[33]. These conditions are met in HPT–processing (see figure 3.5) by putting a disk-shaped sample between two anvils where it is subjected to a pressure in range of several Gigapascals as well a torsional strain ([33],[34]).

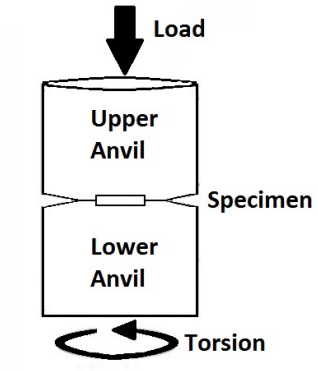

Figure 3.5: Illustration of the principle of HPT

The shear strain γ imposed after N rotations of processing on a sample with Radius r and height h can be calculated from integrating small rotations $d\theta$, with

$\theta = 2\pi N$ to be:

$$\gamma = \frac{2\pi N r}{h} \tag{3.1}$$

To compare HPT with other SPD processes it is useful to calculate a equivalent strain ϵ

$$\epsilon = \frac{1}{a}\gamma \tag{3.2}$$

where the variable a can be chosen according to a criterion of plastic flow (a=2 for Tresca and $\sqrt{3}$ for von Mises) or from the Taylor theory of polycrystals [34].
For this work, XHP Magnesium and 99.95% pure Magnesium were subjugated to HPT–processing under the conditions specified in table 3.2.

Material	Pressure	Rotations	Rotations/min
99.95% Mg	4GPa	2	0.2
99.95% Mg	4GPa	0.125	0.2
XHP Mg	4GPa	2	0.2

Table 3.2: Parameters of HPT–processing

3.2.4 Heat treatment

Heat treatment was performed after HPT–processing and quenching in a silicon oil suitable for high temperatures in a temperature range between 55°C and 190°C. Every sample was heat treated for 10 minutes at the specified temperature and afterward quenched in ice water. The quenched samples which were quenched together from 550°C were also simultaneously aged and quenched in iced water.

3.2.5 Grinding and polishing

Every characterization-method mentioned in chapter 4 requires the specimen to have a smooth, scratch–free surface. Therefore, grinding and polishing are the first -and crucial- steps in specimen preparation.
At first the specimens were ground with two types of abrasive paper made out of SiC_4, that was affixed to a grinding wheel. The abrasive paper used first had a SiC_4 grain size of $155\mu m$, and the grains of the abrasive paper subsequently used had a size of $5\mu m$. During this process the orientation of the specimen was changed multiple times in order to avoid the emerging of a artificial structure. Water was used as anti-blocking agent. After that, the samples were polished with Al_2O_3–paste with grain sizes $1\mu m$ and $0,3\mu m$ on a polishing cloth suitable for soft materials and finally cleansed with isopropanol.

Ion milling

Investigation of samples in a Transmission Electron Microscope (TEM) requires their thickness to be in the range of $\approx$ 200 nm [35]. In order to achieve this thickness, the samples were mechanically ground and polished to $\approx 100 - -150\mu m$ and subsequently ion–milled to electron transparency. When ion milling a specimen, Ar+ ions are fired on it with an energy in the range between 200 eV to 5keV from an angle between 5° and 15° to sample stage surface [35].
For this work, the specimens were thinned and polished with a *Gatan PIPS II* at the *Scientific Center for Optical and Electron Microscopy, ETH Zurich Campus Hoenggerberg.*
A multi-step procedure was carried out in liquid Nitrogen atmosphere, at first thinning the specimen with with acceleration voltages of 4-5 kV and then polishing them with lower acceleration voltages. The exact parameters are given in table 3.3 below.

Material	Step 1: 5keV	Step 2: 4keV	Step 3: 1keV	Step 4: 500eV
CP–Mg	3 hours	2 hours	30 min.	30 min.
Mg–Zn–Ca	5 hours	6 hours	30 min.	30 min.

Table 3.3: Parameters for ion-milling of Magnesium

Chapter 4

Methods of Specimen Characterization

4.1 Microhardness

The main method of characterizing the specimens was measuring the Vickers hardness, a method of static, direct hardness testing [17].
Hardness is defined as the quotient of test force and penetration area determined after the removal of the test force ([17]). The Vickers hardness test, first established in 1922 at the company of the same name ([36],[37]), is specified in ISO 6507–1 (which is followed in this work) and ASTM E 384, respectively.
The indenter used for determining the Vickers hardness has the shape of a pyramid with an opening angle of 136° and is made out of diamond. It is recommended to perform the microhardness test with test forces between 0,09807N and 0,9807 N, which typically are applied for 10s to 15s [1].

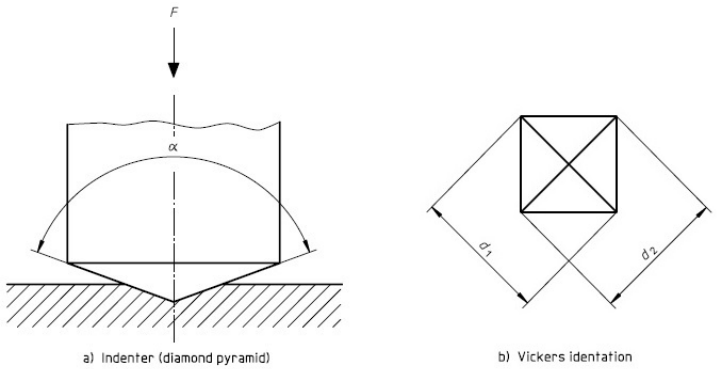

Figure 4.1: principle of the Vickers hardness test [38]

Figure 4.1 shows the the principle and measurement of the Vickers hardness test

[1]Test forces may also be applied longer; this must be mentioned specifically

and 4.2 explains the symbols used in calculating the hardness. The results of such a test are denoted by the symbol HV preceded by the hardness value N followed by the test force F (in kilopond) in the form $N\text{HV}F$. To ensure direct comparability of the obtained values, the parameters of the test should be kept the same for every specimen. For the parameters chosen for this work, see chapter 4.1.3.

α	Angle between the opposite faces at the vertex of the pyramidal indenter (136°)
F	Test force, in newtons
d	Arithmetic mean, in millimeters, of the two diagonals length d_1 and d_2
HV	$\text{Vickers hardness} = \text{Constant} \times \frac{\text{Test force}}{\text{Surface area of indentation}}$ $= 0{,}102 \frac{2F \sin\frac{136°}{2}}{d^2} \approx 0{,}189\,1 \frac{F}{d^2}$

Figure 4.2: Symbols and designations of the Vickers hardness test [38]

A consequence of the definition of hardness is that the quality of the indents is tantamount to the quality (and significance) of the results. Three factors determine the success of the hardness measurement :

1. The shape of the indents
   ...should look like a square on polycrystalline materials. All four, or at least both corners on opposite sites, should have the same height in order to calculate the correct force per area ratio from the diameters.

2. The position of the indents
   The indents should be spread on the specimen in order to get information about the uniformity of the specimen. Nonetheless, more than two indents should be placed in immediate neighborhood to level out statistical mistakes.

3. The number of indents
   Enough indents to calculate statistical parameters should be set, furthermore, the stronger the “natural” fluctuations of the hardness of the specimen are, the more indents should be set.

All of the above mentioned factors are strongly influenced by the surface of the specimen, which should be even and scratch–free to achieve optimal results.
Because of their importance for this work, two extreme cases of specimen–microstructure are now considered.

4.1.1 Coarse–Grained Specimens

If the grain size is large enough for the indents to be smaller than the grains a "single grain" hardness is measured, which poses a problem especially for hexagonally structured materials, which are highly anisotropic with respect to their mechanical properties ([20], [39]). Therefore, a large number of indents should be set across the investigated specimen as shown in figure 4.3.

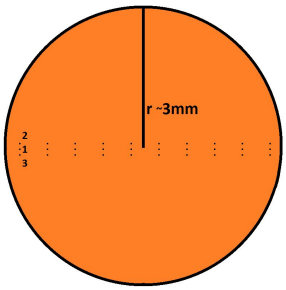

Figure 4.3: Schematic layout of hardness indents in quenched specimens

4.1.2 HPT–Processed Specimens

HPT–processed specimens typically show fine grains [34], smaller than the indent size used in microhardness, but the deformation of the HPT–processed specimen depends on the radius (see equation 3.1). Hence, it is important to always measure at the same radius to ensure the comparability of the results. In this work, as a radius 2 mm from the center was chosen and five indents in the configuration shown in Figure 4.4 were placed at a total of 2 to 4 different places on the specimen.

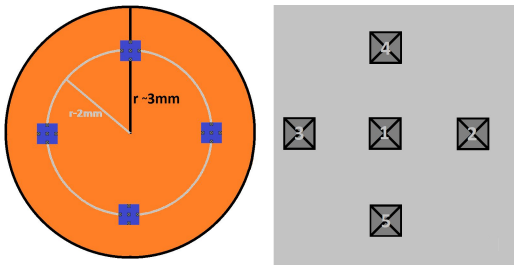

Figure 4.4: Schematic layout of hardness indents on HPT–processed specimens (left) and arrangement of hardness indents (right)

4.1.3 Parameters

The Vickers hardness of all specimens was tested with an *Anton Paar MHT-4 Micro Indentation Tester*, mounted on a *Zeiss Axioplan* miroscope. The indents were evaluated from photos taken with a *Zeiss AxioCam MRc5 5-MP Camera* with the *Zeiss AxioVision 4.8* software in two magnifications, 50x (using a *Epiplan-Neofluar*

50x/0.75 HD DIC and 100x, using a *Epiplan 100x/0.75* objective.
The force used test was chosen according to the *ISO 6507* specifications for microhardness.

Test Force	Time	Gradient
0.2 N	10s	0.01 N/s

Table 4.1: Parameters of the Vickers hardness test

4.1.4 Evaluation of the Results

Single Specimens

For each tested specimen the mean Vickers hardness value of all n indents, $\overline{HV}$, the standard deviation s_{HV} and the mean average error u_{HV} was calculated. Tables of all results can be found in chapter 5.1.

$$\overline{HV} = \sum_{i}^{n} \frac{1}{n} HV_i \tag{4.1a}$$

$$s_{HV} = \sqrt{\frac{1}{n-1} \sum_{i}^{n} \left(HV_i - \overline{HV}\right)^2} \tag{4.1b}$$

$$u_{HV} = \frac{s_{HV}}{\sqrt{n}} \tag{4.1c}$$

Furthermore, a Shapiro–Wilk test of normality – which is well–suited for sample sizes $<$ 50 [40] – was performed with *Wolfram Mathematica 10.1* to make sure the samples used for statistical tests are Gaussian distributed. The significance level was set to be $\alpha = 0,05$.
Additionally, for each specimen histograms were created with *Wolfram Mathematica 10.1*, one with automatically chosen bin widths, which "plots a histogram with equal bin widths chosen to approximate an assumed underlying smooth distribution of the values"[41] and others with manually set bin widths varying from the automatically set one up to 20.

Multiple Specimens

For k specimens prepared in the same way the weighted mean – referred to as $\overline{\mathbf{HV}}$– and the weighted standard deviation – referred to as $\mathbf{\Delta_{HV}}$ – was calculated with weighting coefficients g_j that are indirectly proportional to the mean average error

u_{HV}.

$$\overline{\mathbf{HV}} = \frac{\sum_j^k \overline{HV_j}\, g_j}{\sum_j^k g_j} \tag{4.2a}$$

$$\mathbf{\Delta_{HV}} = \sqrt{\frac{1}{(k-1)} \frac{\sum_j^k \left(\overline{HV_j} - \overline{\mathbf{HV}}\right)^2}{\sum_j^k g_j}} \tag{4.2b}$$

$$g_j = \frac{1}{\left(u_{HV_j}\right)^2} \tag{4.2c}$$

They will be diagrammed in chapter 5.1 in dependence on aging temperature for each material.

T–Test The independent–sample t–test is a two–sample test, which tests if the (unknown) true means μ_1 and μ_2 of a metric, normally distributed characteristic drawn from two disjoint statistical populations match for a predetermined significance level α.[42] Or, expressed in a less mathematical way: are the investigated series of measurement (by chance) drawn from the same statistical population or are there systematic differences in addition to the random sampling uncertainties? [43]

The t–Test compares the mean values and standard deviations via the parameter t, which measures how far apart two means $\overline{x}$ and $\overline{y}$ lie, weighted with the mean error of the difference $d = \overline{x} - \overline{y}$, s_d^2.This parameter is determined by the number of measurements n (corresponding to $\overline{x}$) and m (corresponding to $\overline{y}$) and the individual standard deviations s_x^2 and s_y^2.

$$t = \sqrt{\frac{nm}{n+m}} \frac{\overline{x} - \overline{y}}{s_d} \tag{4.3}$$

$$s_d^2 = \frac{(n-1)s_x^2 + (m-1)s_y^2}{n+m-2} \tag{4.4}$$

The parameter $n + m - 2 \equiv \nu$ is called "degrees of freedom".

Note that t can have a positive as well as negative value, but that the sign is of no consequence for the result of the t–test, as it is not important if $\overline{x}$ is greater than $\overline{y}$ or vice versa.

The starting hypothesis of the test parameter is that the two means are drawn from the same population, for which case the predictand d is zero and the test is fulfilled [43].

The in equation 4.1.4 introduced t is derived from the parameter $\mathfrak{t}$ (equation4.1.4 below), which – per definition – follows Student's t–distribution, by setting $z \equiv \overline{x} - \overline{y}$ and $s_z \equiv s(\overline{x} - \overline{y})$. The probability density function of Student's t–distribution

$\phi(\mathfrak{t}, \nu)$ is given in equation 4.1.4, where ν are the above mentioned degrees of freedom and Γ is the gamma function.

$$\mathfrak{t} = \frac{z - \overline{z}}{s_z} \tag{4.5}$$

$$\phi(\mathfrak{t}, \nu) = \frac{\Gamma((\nu + 1))/2}{\sqrt{\pi\nu}\Gamma(\nu/2)(1 + \mathfrak{t}^2/\nu)^{(\nu+1)/2}} \tag{4.6}$$

For $\nu \to \infty$ the t–distribution will follow a Gaussian distribution. The cumulative distribution function $T(\mathfrak{t}, \nu)$ is the probability to find t-values that lie outside a confidence interval $\pm\ t$ in absence of systematical errors [43].

$$T(\mathfrak{t}, \nu) = \int_{-\infty}^{-\mathfrak{t}} \phi d\mathfrak{t}' + \int_{+\infty}^{+\mathfrak{t}} \phi d\mathfrak{t}' \tag{4.7}$$

The values of $T(\mathfrak{t}, \nu)$ and/or the corresponding quantity $p = 1 - -T$ for different $\mathfrak{t}$ and ν have to be looked up in tables or can be obtained by using a statistic's program and are then compared to a predetermined confidence level α, which often is set to be 5% or 1% [2]

To report the results of a t–test, the American Psychological Association (APA) recommends to provide the parameters t and p, presenting them in the following style: "There was a significant/not significant difference for condition 1 ($\overline{x} =$, $s_x =$) and condition 2 ($\overline{y} =$, $s_y =$); $t(\nu) =$, $p =$."

To assess if there is a statistically significant difference between the results of different specimen treatments, an independent–samples t-test was performed with *IBM SPSS Statistics Version 23* with a confidence level set to be 5%. The mean Vickers hardness of k specimens treated the same way as calculated by *SPSS* to perform an independent samples t-test is referred to as HV^m and the corresponding standard deviation as s^m_{HV}.

$$HV^m = \sum_j^k \frac{1}{k} \overline{HV_j} \tag{4.8a}$$

$$s^m_{HV} = \sqrt{\frac{1}{(k-1)} \sum_j^k \left(\overline{HV_j} - HV^m\right)^2} \tag{4.8b}$$

[2] note that, for a Guassian distribution, 95% of all measurements deviate 1,96 σ at maximum and 99% of all measurements deviate 2,576 σ at maximum from the mean.

4.2 Electron Microscopy

4.2.1 Transmission Electron Microscopy

The principle of a Transmission Electron Microscope (TEM) is the same as the principle of a light microscope, with the obvious "replacement" of light waves by electron waves in order to achieve a higher resolution. If one considers the resolution according to Abbe's theorem

$$d = 0.61\frac{\lambda}{nsin\alpha} \tag{4.9}$$

where d denotes the minimal resolved distance resolvable in a medium with refraction index n generated by an objective with opening aperture 2α using a (light) wave with wavelength λ. The wavelength of visible light approximately lies between 400 nm and 700 nm, whereas the wavelength λ_{el} of electrons depends on their momentum p (and therefore their kinetic energy E_{kin}) according to deBroglie's relation

$$\lambda_{el} = \frac{h}{p} = \frac{h}{\sqrt{2mE_{kin}}} = \frac{h}{\sqrt{2meU}} \tag{4.10}$$

One can substitute for the mass of the electron m, Planck's constant h and the elementary charge e leading to an approximation for the electron wavelength only dependent on the acceleration voltage U

$$\lambda_{el} = \frac{1,23}{\sqrt{U}} \quad (nm) \tag{4.11}$$

One can easily see that a resolution in the orders of 0,2 nm could – theoretically – be reached. However, the electron beam requires not glass, but electromagnetic lenses, which leads to aberrations that limit the resolution and quality of the pictures. Bright field micrographs for this work were taken using a (S)TEM *FEI Talos F200X (Chem S/TEM)* at ETH Zuerich–Hoenggerberg in cooperation with R.Schaeublin.

4.2.2 Scanning Electron Microscopy

The Scanning Electron Microscope (SEM) is a versatile instrument to characterize various properties of different (conductive) materials. These properties include information about the surface structure, elemental composition and texture of the investigated specimen. In a SEM, a small–sized electron probe scans the surface of the specimen thus allowing a point–wise collection of information gathered from the electron probe–specimen interaction.
The resolution mainly depends on the kinetic energy of the electrons hitting the

surface, the type and the geometry of the specimen as well as the atomic numbers of the atoms present in the specimen. SEMs can achieve a resolution in the range of nanometers [44].

Information gathering from the SEM

When highly energetic electrons hit the surface of a specimen, they interact with the atoms in several ways, which leads to different effects:

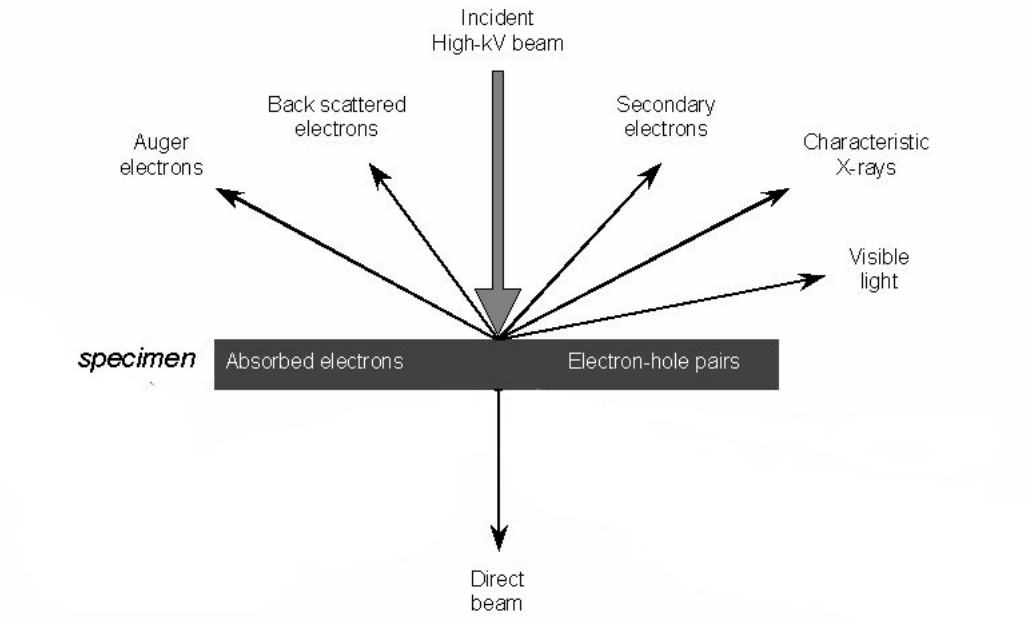

Figure 4.5: Overview of the information gathered from SEM

In the following an overview of the relevant processes is given ([46],[45]):

1. Secondary electrons
   Collecting Secondary Electrons is the most common imaging method. They are ejected from lower shells (usually the K shell) of the atoms by inelastic scattering with the beam electrons (=primary particles).Since they are not high in energy ($\approx$ 5 eV) the depth of information is only $\approx$ 10 nm and thus they can only give information about the surface.

2. Backscattered electrons (BSE)
   are reflected primary electrons and very high in energy (approximately the energy of the incoming beam). Images obtained through backscattered electrons display atomic number contrast with brighter regions being generated from

areas of higher atomic number. Grain contrast imaging is also possible with BSE.

3. Electron backscatter diffraction (EBSD)
   Kikuchi bands – the results of inelastic scattering of electrons – can give information about the orientation of crystals and are used in to get information about grain sizes and texture. For this, the specimen is tilted by angles of typically 60° to 70° in order to allow more electrons to be diffracted and to escape towards the detector. Then, for each point of the specimen, a Kikuchi pattern is recorded and the crystal orientation is calculated from the positions of the Kikuchi band by computer processing of digitized diffraction pattern.

4. X-rays
   Primary particles directly interact with shell electrons in way that an electron gets enough energy to leave its shell (ionisation). The generated hole will be immediately occupied from an electron of an outer-shell, thereby loosing a characteristic quantum of energy. Detecting these via energy–dispersive (EDX) or wavelength–dispersive (WDX) spectroscopy gives information about the sort of atoms in the specimen.

Scanning Electron Microscopy was employed in this work to determine the grain size and texture via EBSD and BSE with a *Zeiss Supra 55 VP*.
The grain area was determined using *ImageJ 1.47V*; assuming the area to be of circular shape allowed the calculation of an average radius.

4.2.3 Scanning Transmission Electron Microscopy (STEM)

The basic principle of a STEM is to combine the advantages of Scanning- and Transmission Electron Microscopy: A electron beam is focused to a small probe size and is raster scanned in parallels across the surface of the investigated specimen while transmitting it. Depending on the probe size of the beam and the thickness of the specimen even atomic resolution can be achieved [17].
With using a High Angle Annular Dark Field (HAADF)-Detector spatially resolved information about the elements in the investigated specimen can be obtained. A fraction of the incident electrons is scattered by thermal vibrations of the atoms in the (crystalline) specimen, where atoms with a high atomic number scatter the electrons at larger angles than atoms with a small atomic number ("Z-Contrast") and collected at the back focal plane by the HAAADF-Detector, where heavier elements contribute to brighter contrast. The observed angles are – with typically being ≈ 70 mrad – large compared to the angles usually observed in electron microscopy.[17].
Energy-dispersive X-ray spectrometry can also be carried out in a STEM and follows

the same principles as explained in chapter 4.2.2 (above). For this work, HAADF–STEM and STEM–EDS images were taken with a *FEI Talos F200X (Chem S/TEM)* equipped with a *Super-X EDS system* at ETH Zuerich–Hoenggerberg in cooperation with R.Schaeublin.

Chapter 5

Results

In the first part of this chapter the results of the Vickers hardness (HV) measurements will be reported. Every specimen was either quenched from 550° C and subsequently aged for 10 minutes **or** HPT–processed and subsequently aged for 10 minutes.
The mean Vickers hardness $\overline{HV0.02}$, the corresponding standard deviation s_{HV} and the mean average error u_{HV} was determined for each specimen afterward.
Furthermore, the mean Vickers hardness $HV0.02^m$ and the corresponding standard deviation s^m_{HV} of all identically treated specimens will be reported when an independent samples t-test was performed. The significance level of the independet samples t-test is $\alpha = 5\%$ [1].
The weighted mean Vickers hardness ***HV0.02*** and the corresponding weighted standard deviation$\mathbf{\Delta_{HV}}$ will be diagrammed in dependence on aging temperature.
For a detailed explanation of the mentioned quantities the reader is referred to chapter 4.1.4.

5.1 Microhardness

5.1.1 Quenched Specimens

A characteristic of all quenched specimens are coarse grains (see 5.2.2 for more information), therefore the procedure outlined in 4.1.1 was followed to determine their Vickers hardness HV.

CP–Magnesium

In total 44 specimens, of which 22 showed obvious traces of oxidation after quenching, were prepared. The oxidized specimens were characterized nonetheless, but are

[1] i.e. that results are not considered statistically significant if $p < \alpha$

to be considered separately.
Table 5.1 shows the individual results of each quenched specimen without any visible traces of oxidation and figure 5.1 shows the weighted means ***HV0.02*** and weighted standard deviations $\mathbf{\Delta_{HV}}$ plotted against the temperature of the heat treatment.

Sample Name	**Aging**	$\overline{\mathbf{HV0.02}}$	$\pm\mathbf{s_{HV}}$	u_{HV}
030915_99.95_550q_1	none	34,5	4,3	0,8
030915_99.95_550q_2	none	34,7	3,9	0,7
040915_99.95_550q_1	none	33,8	3,9	0,8
040915_99.95_550q_2	none	36,6	3,2	0,6
020915_99.95_550q_90C_10_1	10min at 90°C	37,6	2,3	0,4
020915_99.95_550q_90C_10_2	10min at 90°C	36,6	2,4	0,4
070915_99.95_550q_90C_10_1	10min at 90°C	35,5	3	0,5
070915_99.95_550q_90C_10_2	10min at 90°C	38,6	2,4	0,4
110915_99.95_550q_90C_10_1	10min at 90°C	37,2	3,1	0,5
110915_99.95_550q_90C_10_2	10min at 90°C	41,7	3,8	0,7
020915_99.95_550q_110C_10_1	10min at 110°C	35,7	3,8	0,7
020915_99.95_550q_110C_10_2	10min at 110°C	36,2	3,2	0,6
080915_99.95_550q_110C_10_1	10min at 110°C	38,3	3,7	0,6
080915_99.95_550q_110C_10_2	10min at 110°C	34,4	2,9	0,5
010915_99.95_550q_130C_10_1	10min at 130°C	35	2,6	0,5
010915_99.95_550q_130C_10_2	10min at 130°C	33,7	3,7	0,7
090915_99.95_550q_130C_10	10min at 130°C	35,0	3,2	0,6
280815_99.95_550q_150C_10_1	10min at 150°C	35,2	3,4	0,6
280815_99.95_550q_150C_10_2	10min at 150°C	34,8	2,4	0,4
090915_99.95_550q_150C_10_1	10min at 150°C	33,6	3,8	0,7
090915_99.95_550q_150C_10_2	10min at 150°C	35,5	3,4	0,6
270815_99.95_550q_170C_10_1	10min at 170°C	36,3	5,6	1,0
270815_99.95_550q_170C_10_2	10min at 170°C	33,9	3,4	0,6

Table 5.1: Individual results of the Vickers hardness test of non-oxidized quenched CP–Mg specimens

It is discernible from figure 5.1 that the maximum increase in HV occurs when the specimens are aged for 10 min. at 90° C.
To assess the increase in HV, an independent samples t-test was conducted comparing the HV of solely quenched and additionally at 90°C aged specimens. There is a significant difference in the $HV0.02^m$ values for solely quenched ($HV0.02^m$ = 34,9 s^m_{HV} = 1,2) and quenched/at 90°C aged ($HV0.02^m$ = 37,9 s^m_{HV} = 2,1) specimens; t(8) = 2,49, p = 0,038. A significant drop in HV occurs after aging for 10 min. at 130°C ($HV0.02^m$ = 34,57 s^m_{HV} = 0,75) compared to the maximum HV; t(7)=2,156, p=0,04.
With reference to the weighted mean ***HV0.02*** of the quenched specimens, the HV increases by $\approx$ 7 %.

Table 5.2 shows the individual results of the during quenching oxidized specimens

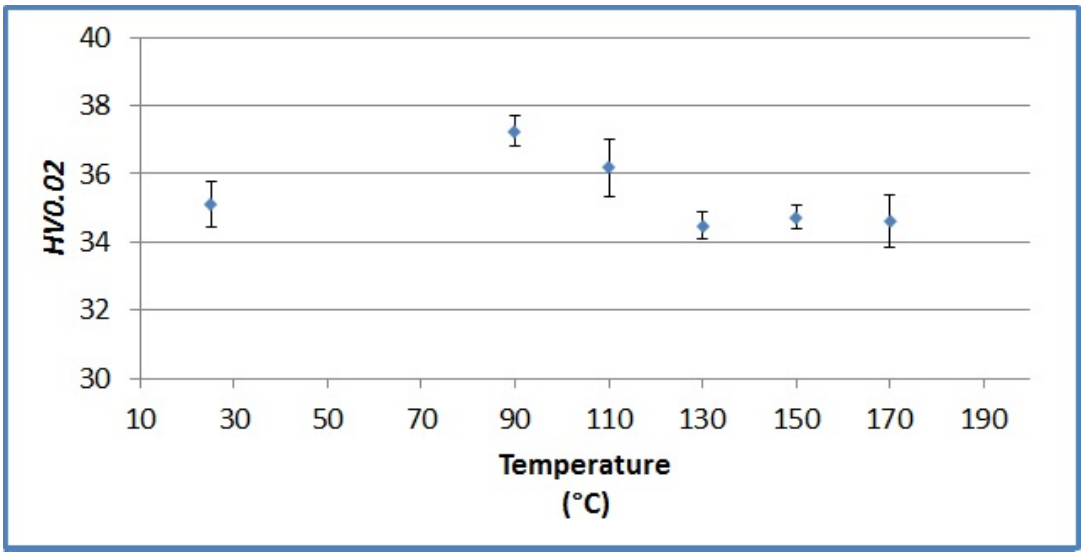

Figure 5.1: Isochronal hardness curve as a function of temperature (aging time: 10min) for non–oxidized CP–Mg quenched from 550°C; error bar indicate $\mathbf{\Delta_{HV}}$

and figure 5.2 the weighted means ***HV0.02*** and weighted standard deviations $\mathbf{\Delta_{HV}}$ plotted against the aging temperature.

Sample Name	**Aging**	$\overline{\mathbf{HV0.02}}$	$\pm s_{HV}$	u_{HV}
030614_99.95_550q	none	48,6	4,3	1,1
030614_99.95_550q	none	43,7	2,5	0,8
190814_99.95_550q	none	45,00	3,8	0,7
220714_99.95_550q_1	none	38,4	2,9	0,8
220714_99.95_550q_2	none	50,9	6,4	1,6
240714_99.95_550q_2	none	42,3	4,7	1,1
190814_99.95_550q_130C_10_1	10min at 130°C	49,4	5,3	1,0
190814_99.95_550q_130C_10_2	10min at 130°C	46,1	4,3	0,8
090714_99.95_550q_150C_10_1	10min at 150°C	52,5	7,2	2,3
090714_99.95_550q_150C_10_2	10min at 150°C	54,6	8,7	2,8
100714_99.95_550q_150C_10_1	10min at 150°C	52,6	7,3	1,9
100714_99.95_550q_150C_10_2	10min at 150°C	43,0	6,2	1,6
110714_99.95_550q_150C_10_2a	10min at 150°C	51,6	3,8	1,2
110714_99.95_550q_150C_10_2b	10min at 150°C	41,8	4,6	1,5
140814_99.95_550q_150C_10	10min at 150°C	41,2	5,2	1,1
190814_99.95_550q_150C_10	10min at 150°C	49,5	3,0	0,6
140814_99.95_550q_170C_10	10min at 170°C	49,6	5,0	1,2
180614_99.95_550q_170C_10_1	10min at 170°C	46,7	3,6	0,9
180614_99.95_550q_170C_10_2	10min at 170°C	56,6	3,4	0,9
080714_99.95_550q_170C_10_1	10min at 170°C	42,9	2,1	0,7
080714_99.95_550q_170C_10_2	10min at 170°C	56,5	4,3	1,4
220814_99.95_550q_190C_10	10min at 190°C	42,5	3,0	0,5
190814_99.95_550q_190C_10	10min at 190°C	48,4	3,4	0,7

Table 5.2: Individual results of the Vickers hardness test of oxidized quenched CP–Mg specimen

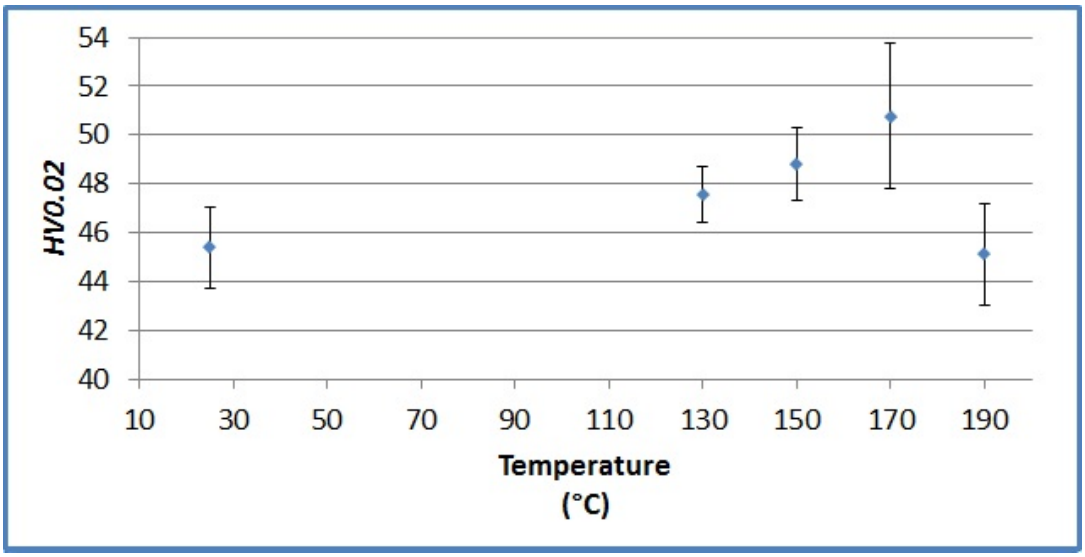

Figure 5.2: Isochronal hardness curve as a function of temperature (aging time: 10min) for oxidized CP–Mg quenched from 550°C; error bars indicate $\mathbf{\Delta_{HV}}$

It can be gathered from figure 5.2 that the maximum HV occurs in the course of aging the quenched specimens at 170° C for 10 min. and gives an increase of ≈ 12 % compared to the ***HV0.02*** of solely quenched specimens. However, the measurement error is large compared to the non–oxidized specimens and the conducted independent–samples t-test to compare the HV of purely quenched ($HV0.02^m$ = 44,8 s^m_{HV} = 4,5) and additionally for 10 min. at 170° aged ($HV0.02^m$ = 50,5 s^m_{HV} = 6) specimens gave the result of t(9)=1,781, p=0,102. Usually, only tests with a p–value of 0,05 or smaller are considered significant, however, in cases with small populations values of p=0,10 may also be deemed significant. For the results of the oxidized specimens the only independent samples t-test that could be considered significant is the presented case, all others showed results with p–values larger than 0,102 and were therefore deemed not significant.

Magnesium–Zinc

In total 23 specimens were investigated, of which the individual Vivkers hardness values are given in table 5.3.

Figure5.3 shows the weighted means ***HV0.02*** and weighted standard deviation $\mathbf{\Delta_{HV}}$ of the Vickers hardness values plotted against the aging temperature.

Name	Aging	$\overline{HV0.02}$	s_{HV}	u_{HV}
201114_MgZn_550q	none	41,1	2,3	0,4
211114_MgZn_550q_1	none	40,7	3,2	0,5
211114_MgZn_550q_2	none	38,5	3,2	0,7
201114_MgZn_550q_90C_10_1	10min at 90°C	38,4	2,9	0,5
201114_MgZn_550q_90C_10_2	10min at 90°C	41,1	5,4	0,9
010615_MgZn_550q_90C_10_1	10min at 90°C	41,0	4,0	0,7
010615_MgZn_550q_90C_10_2	10min at 90°C	39,6	2,6	0,5
241114_MgZn_550q_110C_10_1	10min at 110°C	41	3,7	0,7
241114_MgZn_550q_110C_10_2	10min at 110°C	42,1	4,5	0,8
191114_MgZn_550q_130C_10_1	10min at 130°C	46,2	3,5	0,6
191114_MgZn_550q_130C_10_2	10min at 130°C	44,3	3,5	0,6
011214_MgZn_550q_130C_10_1	10min at 130°C	44,6	4,8	0,8
011214_MgZn_550q_130C_10_2	10min at 130°C	40,9	3,9	0,7
251114_MgZn_550q_150C_10_1	10min at 150°C	40,8	4,3	0,7
251114_MgZn_550q_150C_10_2	10min at 150°C	41,4	3	0,5
191114_MgZn_550q_170C_10_1	10min at 170°C	42,3	2,9	0,5
191114_MgZn_550q_170C_10_2	10min at 170°C	44,6	3,9	0,7
270515_MgZn_550q_170C_10_1	10min at 170°C	43,9	4,2	0,7
270515_MgZn_550q_170C_10_2	10min at 170°C	39,9	3,0	0,5

Table 5.3: Individual results of the Vickers hardness test of non-oxidized quenched Mg–Zn specimens

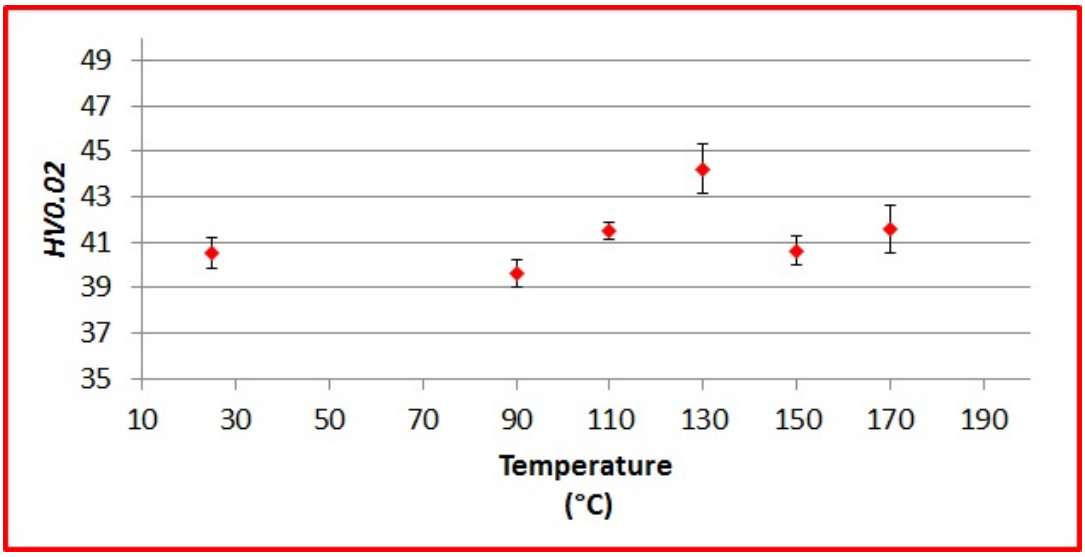

Figure 5.3: Isochronal hardness curve as a function of temperature (aging time: 10min) for Mg–Zn quenched from 550°C; error bars indicate $\mathbf{\Delta_{HV}}$

It can be recognized from figure 5.3 that the maximum increase in HV occurs in the course of aging the quenched specimens for 10 min. at 130° C.
To assess the increase in HV, an independent samples t-test was conducted to compare the Vickers hardness of solely quenched and additionally for 10 min. at 130° C aged specimens. There is a significant difference in the $HV0.02^m$ of solely quenched

($HV0.02^m$ = 40,1 s^m_{HV} = 1,4) and quenched/at 130° C aged ($HV0.02^m$ = 44,0 s^m_{HV} = 2,2) specimens; t(5)=2,627 , p=0,049. This also holds true for the difference between the maximum $HV0.02^m$ and the for 10 min. at 90° C aged specimens ($HV0.02^m$= 40,0 s^m_{HV}= 1,3; t(6) = 3,115 , p = 0,021).
With reference to the ***HV0.02*** of the quenched specimens the increase in HV is ≈ 9 %.

Magnesium–Zinc–Calcium

In total 26 specimens were investigated of which the individual Vickers hardness values are given in table 5.4. For calculating the weighted means ***HV0.02*** and weighted standard deviations $\mathbf{\Delta_{HV}}$ the specimens *290615-MgZnCa550q-130C-10-1*, *290615-MgZnCa-550q-130C-10-2* , *150915-MgZnCa-550q-150C-10-1* and *150915-MgZnCa-550q-150C-10-2* had to be excluded, as they were ≈ 15% thicker than the other specimens, which led to a slower cooling rate during quenching. Figure 5.4 shows the weighted means ***HV0.02*** of the other Vickers hardness values plotted against the aging temperature.

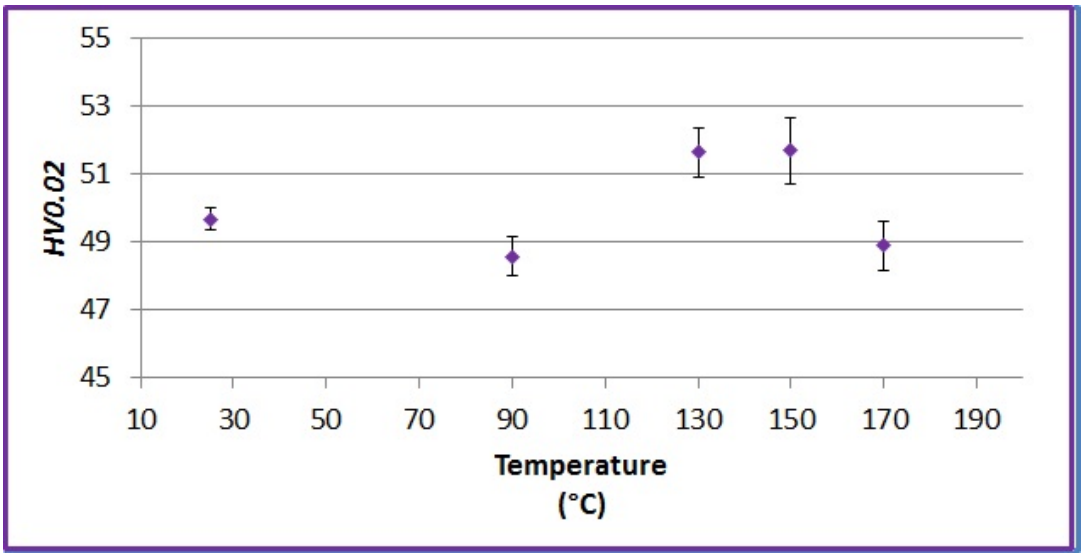

Figure 5.4: Isochronal hardness curve as a function of temperature (aging time: 10min) for Mg–Zn–Ca quenched from 550°C; error bars indicate $\mathbf{\Delta_{HV}}$

Name	**Aging**	$\overline{\boldsymbol{HV0.02}}$	$\boldsymbol{s_{HV}}$	$\boldsymbol{u_{HV}}$
020615_MgZnCa_550q_1	none	50,0	4,4	0,9
020615_MgZnCa_550q_2	none	50,5	4,2	0,9
090615_MgZnCa_550q_1	none	49,0	3,6	0,7
090615_MgZnCa_550q_2	none	49,8	4,8	0,9
120615_MgZnCa_550q_90C_10_1	10min at 90°C	49,6	3,4	0,6
120615_MgZnCa_550q_90C_10_2	10min at 90°C	47,2	3,4	0,6
300615_MgZnCa_550q_90C_10_1	10min at 90°C	50,0	5,1	1,0
300615_MgZnCa_550q_90C_10_2	10min at 90°C	48,4	2,7	0,5
100615_MgZnCa_550q_130C_10_1	10min at 130°C	54,0	4,3	0,8
100615_MgZnCa_550q_130C_10_2	10min at 130°C	53,3	3,4	0,7
290615_MgZnCa_550q_130C_10_1	10min at 130°C	47,3	3,7	0,7
290615_MgZnCa_550q_130C_10_2	10min at 130°C	46,1	3,7	0,7
020715_MgZnCa_550q_130C_10_1	10min at 130°C	51,1	3,6	0,7
020715_MgZnCa_550q_130C_10_2	10min at 130°C	50,7	3,1	0,7
030715_MgZnCa_550q_130C_10_1	10min at 130°C	49,6	4,4	0,8
030715_MgZnCa_550q_130C_10_2	10min at 130°C	49,9	4,6	0,8
180615_MgZnCa_550q_150C_10_1	10min at 150°C	53,6	4,0	0,7
180615_MgZnCa_550q_150C_10_2	10min at 150°C	49,4	3,1	0,6
190615_MgZnCa_550q_150C_10_1	10min at 150°C	52,9	3,2	0,6
190615_MgZnCa_550q_150C_10_2	10min at 150°C	51,4	3,8	0,7
150915_MgZnCa_550q_150C_10_1	10min at 150°C	49,9	4,4	0,7
150915_MgZnCa_550q_150C_10_2	10min at 150°C	50,6	4,4	0,8
110615_MgZnCa_550q_170C_10_1	10min at 170°C	48,9	3,2	0,6
110615_MgZnCa_550q_170C_10_2	10min at 170°C	47,8	5,0	0,9
220615_MgZnCa_550q_170C_10_1	10min at 170°C	47,7	3,1	0,6
220615_MgZnCa_550q_170C_10_2	10min at 170°C	50,7	3,6	0,6

Table 5.4: Individual results of the Vickers hardness test of non-oxidized quenched Mg–Zn–Ca specimens

It is discernible from figure 5.3 that the maximum increase in HV occurs in the course of aging the specimens for 10 min. at 130° C or 10 min. at 150° C.
A independent samples t-test, conducted to assess the difference in HV between the solely quenched specimens ($HV0.02^m = 49{,}83$ $s^m_{HV} = 0{,}62$) and the additionally at 130° C ($HV0.02^m = 51{,}4$ $s^m_{HV} = 1{,}8$) or at 150° C ($HV0.02^m = 51{,}8$ $s^m_{HV} = 1{,}6$) aged specimens, respectively, yielded ambiguous results that did not allow an assessment of a significant maximum. However, if an independent samples t-test is conducted to determine the significance of the difference in HV of the at 170° C aged specimens and the at 130° C, with t(8) = 2,504 , p = 0,37, and 150° C aged specimens, with t(6)=2,691 ,p=0,36, the results show that the maximum $HV0.02^m$ is statistically significant. With reference to the ***HV0.02*** of the solely quenched specimens the increase in HV is ≈ 5 %.

5.1.2 HPT–Processed Specimens

CP–Magnesium

Two different deformation parameters were chosen for the CP–Mg specimens (see table 3.2).

0.125 Rotations CP–Mg was HPT–processed by 0,125 rotations at a pressure of 4 GPa and the Vickers hardness was determined as outlined in chapter 4.1.2, corresponding to $\gamma \approx 3$. In total 20 specimens were investigated of which the individual Vickers hardness values are given in table 5.5.

Sample Name	**Aging**	$\overline{\mathbf{HV0.02}}$	$\pm s_{HV}$	u_{HV}
101114_99.95_HPT37	none	39,4	4,2	0,9
101114_99.95_HPT38	none	42,7	2,7	0,6
111114_99.95_HPT39	none	43,2	4,5	1,0
111114_99.95_HPT40	none	42,6	2,4	0,5
020215_99.95_HPT68	none	39,9	3,6	0,8
020215_99.95_HPT69	none	38,4	5,3	1,2
210415_99.95_HPT71	none	44,2	3,9	0,9
210415_99.95_HPT72	none	45,4	2,9	0,7
121114_99.95_HPT43_90C_10_1	10min at 90°C	41,3	3,4	0,6
121114_99.95_HPT44_90C_10_2	10min at 90°C	41,8	3,1	0,6
080115_99.95_HPT60_90C_10_1	10min at 90°C	36,3	2,7	0,6
080115_99.95_HPT61_90C_10_2	10min at 90°C	37,6	2,3	0,6
271114_99.95_HPT45_110C_10_1	10min at 110°C	41,4	3,5	0,6
271114_99.95_HPT46_110C_10_2	10min at 110°C	40,1	2	0,4
111114_99.95_HPT41_130C_10_1	10min at 130°C	39,7	2	0,5
111114_99.95_HPT42_130C_10_2	10min at 130°C	39,6	3,5	0,9
281114_99.95_HPT47_150C_10_1	10min at 150°C	41,1	3,4	0,8
281114_99.95_HPT48_150C_10_2	10min at 150°C	37,3	3,3	0,7
070115_99.95_HPT58_150C_10_1	10min at 150°C	40,5	2,8	0,6
070115_99.95_HPT59_150C_10_2	10min at 150°C	39,0	3,3	0,7

Table 5.5: Individual results of the Vickers hardness test of CP–Mg specimens HPT–processed by $\gamma \approx 3$

Figure5.6 shows the weighted means ***HV0.02*** and weighted standard deviations $\mathbf{\Delta_{HV}}$ plotted against the aging temperature. Of the eight investigated solely HPT–processed specimens three failed the Shapiro–Wilk test for normality, which made further investigations necessary. If the intervals are chosen sufficiently fine, the histograms of all solely HPT–processed specimens show a bimodal distribution, particularly strong developed in the specimens that failed the Shapiro–Wilk test. As a representative example the histogram of specimen *101114-99.95-HPT38* is shown in figure 5.5.

The values for the standard deviation for the specimens *101114-99.95-HPT38*, *101114-*

99.95-HPT38 and *101114-99.95-HPT38* are therefore to be understood in a purely mathematical way, as the standard deviation is only defined for normal distributions.

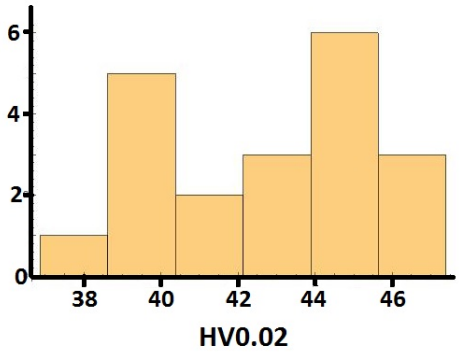

Figure 5.5: Representative histogram of CP–Mg HPT–processed by $\gamma \approx 3$

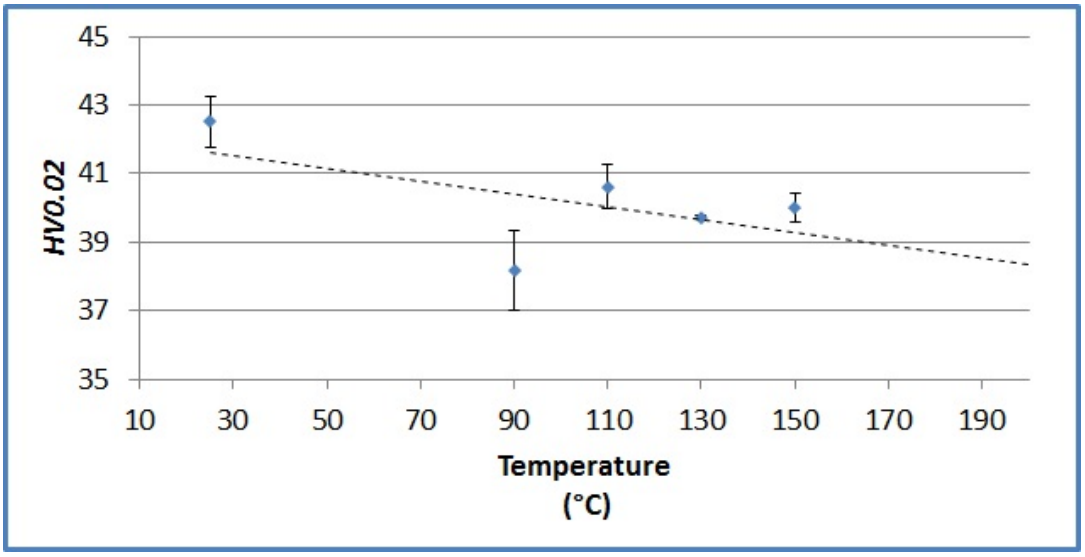

Figure 5.6: Isochronal hardness curve as a function of temperature (aging time: 10min) for CP–Mg HPT–processed by $\gamma \approx 3$; error bars indicate $\mathbf{\Delta_{HV}}$

It is discernible from figure 5.6 that **no** increase in HV occurs in the course of aging the specimens after HPT–processing with respect to the solely HPT–processed specimens. While it may appear that there is at first a drop in HV from the HPT–processed specimens in comparison to the after HPT–processing for 10 min. at 90°C aged specimens and a subsequent rise in HV if the at 90° C aged specimens are compared to the at 110°C aged specimens, an independent samples t-test shows that there is no statistically significant difference in $HV0.02^m$between at 90°C ($HV0.02^m$ = 39,3 s^m_{HV} = 2,7) and at 110° C ($HV0.02^m$ s^m_{HV} = 0,92) aged specimens; t(3,916) = 0,996 ,p = 0,377.

2 Rotations In total 35 specimens were investigated as outlined in chapter 4.1.2 after HPT–processing by 2 rotations at 4 GPa, corresponding to $\gamma \approx 50$. of The

results of the Vickers hardness tests for each specimen are given in table 5.6. Figure5.7 shows the weighted means ***HV0.02*** and weighted standard deviations $\mathbf{\Delta_{HV}}$ of the Vickers hardness values plotted against the aging temperature.

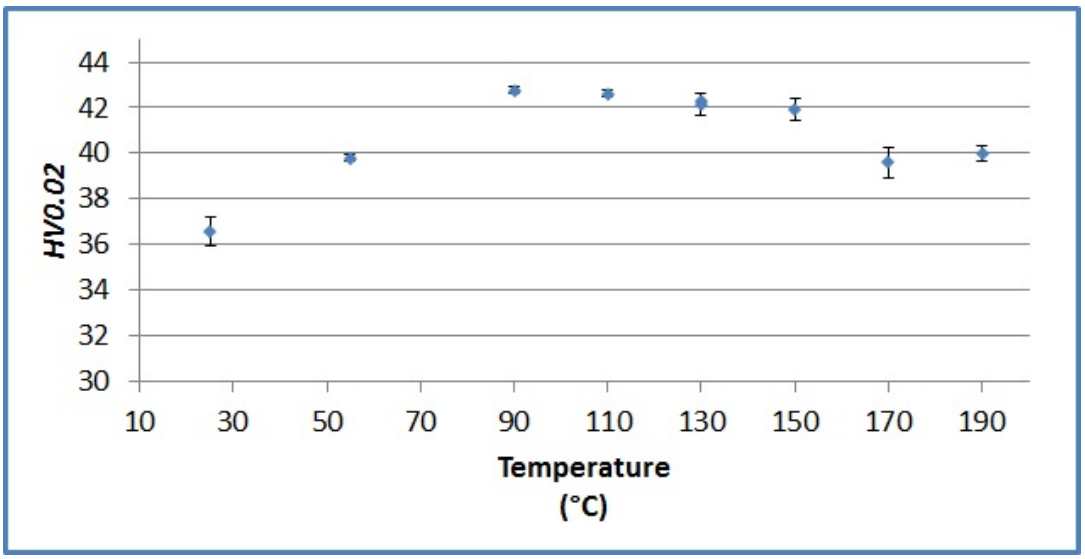

Figure 5.7: Isochronal hardness curve as a function of temperature (aging time: 10min) for CP–Mg HPT–processed by $\gamma \approx 50$; error bars indicate $\mathbf{\Delta_{HV}}$

It is discernible from figure 5.7 that an increase in HV by $\approx 17\%$ occurs in the course of aging specimens at 90°C. The independent samples t-test conducted to compare the two conditions suggest that there is a significance difference in $HV0.02^m$ for HPT–processed ($HV0.02^m$ = 37,4 $\mathbf{s_{HV}} = 2,6$) and additionally at 90° aged ($HV0.02^m$ = 42,70 $\mathbf{s_{HV}} = 0,29$) specimens, t(7) = 3,953 ; p = 0,006.
Aging for 10 min. at 170° C seems to cause a drop in HV, a result supported by the independent samples t–test conducted for HPT–processed and additionally at 150°C aged ($HV0.02^m$ = 41,9 $\mathbf{s_{HV}} = 1$) and HPT–processed/at 170°C aged specimens ($HV0.02^m$ = 40,53 $\mathbf{s_{HV}} = 0,38$) specimens, t(3,776) = 2,439 ; p = 0,075.

Sample Name	**Aging**	$\overline{\mathbf{HV0.02}}$	$\pm\mathbf{s_{HV}}$	$\boldsymbol{u_{HV}}$
010914_99.95_HPT2	none	37,3	0,9	0,2
061114_99.95_HPT36	none	36,6	0,5	0,1
091214_99.95_HPT52	none	36	0,9	0,2
091214_99.95_HPT53	none	35,2	0,9	0,2
190815_99.95_HPT73_55C_10	10min at 55°C	40,1	2,1	0,5
190815_99.95_HPT76_55C_10	10min at 55°C	39,6	1,7	0,4
191214_99.95_HPT56_90C_10	10min at 90°C	42,4	2,4	0,6
191214_99.95_HPT57_90C_10	10min at 90°C	43,0	2,6	0,4
090115_99.95_HPT62_90C_10	10min at 90°C	42,5	2,2	0,5
090115_99.95_HPT63_90C_10	10min at 90°C	42,9	2,2	0,5
230914_99.95_HPT23_110C_10	10min at 110°C	42,7	2,7	0,7
230914_99.95_HPT24_110C_10	10min at 110°C	42,5	1,8	0,5
171214_99.95_HPT54_110C_10	10min at 110°C	42,9	1,9	0,4
171214_99.95_HPT55_110C_10	10min at 110°C	42,1	2,6	0,7
29.08.14_99.95_HPT1_130C_10	10min at 130°C	41,3	2,4	0,6
09.09.14_99.95_HPT7_130C_10	10min at 130°C	43,4	2,5	0,6
160914_99.95_HPT17_130C_10	10min at 130°C	42,9	2,5	0,7
160914_99.95_HPT18_130C_10	10min at 130°C	41,6	1,8	0,5
090914_99.95_HPT6_150C_10	10min at 150°C	42,8	1,7	0,4
090914_99.95_HPT8_150C_10	10min at 150°C	42,7	2,4	0,6
170914_99.95_HPT19_150C_10	10min at 150°C	40,7	2,3	0,6
170914_99.95_HPT20_150C_10	10min at 150°C	41,3	1,8	0,5
10.09.14_99.95_HPT9_170C_10	10min at 170°C	38,4	3,5	0,9
10.09.14_99.95_HPT10_170C_10	10min at 170°C	37,3	2,5	0,7
120914_99.95_HPT13_170C_10	10min at 170°C	41,0	2,4	0,6
120914_99.95_HPT14_170C_10	10min at 170°C	40,4	2,3	0,6
220115_99.95_HPT66_170C_10	10min at 170°C	40,1	3,1	0,7
220115_99.95_HPT67_170C_10	10min at 170°C	40,6	2,5	0,6
100914_99.95_HPT11_190C_10	10min at 190°C	38,8	3,7	0,7
100914_99.95_HPT12_190C_10	10min at 190°C	40,2	4,0	0,7
150914_99.95_HPT15_190C_10	10min at 190°C	42,2	3,6	1,0
150914_99.95_HPT16_190C_10	10min at 190°C	40,3	2,2	0,6
210115_99.95_HPT64_190C_10	10min at 190°C	39,5	2,5	0,6
210115_99.95_HPT65_190C_10	10min at 190°C	39,7	2	0,5

Table 5.6: Individual results of the Vickers hardness test for CP–Mg HPT–processed by $\gamma \approx 50$

XHP – Magnesium

In total 20 specimens were investigated following the procedure outlined in4.1.2 after HPT–processing by 2 rotations at 4 GPa, corresponding to $\gamma \approx 50$. The results of the Vickers hardness tests for each specimen are given in table 5.7. Figure 5.8 shows the weighted means ***HV0.02*** and weighted standard deviations $\boldsymbol{\Delta_{HV}}$ of the HV values plotted against the aging temperature.

It is discernible from figure 5.8 that an increase in HV occurs in the course of aging the HPT–processed specimens for 10 min. at 110°C . With reference to the

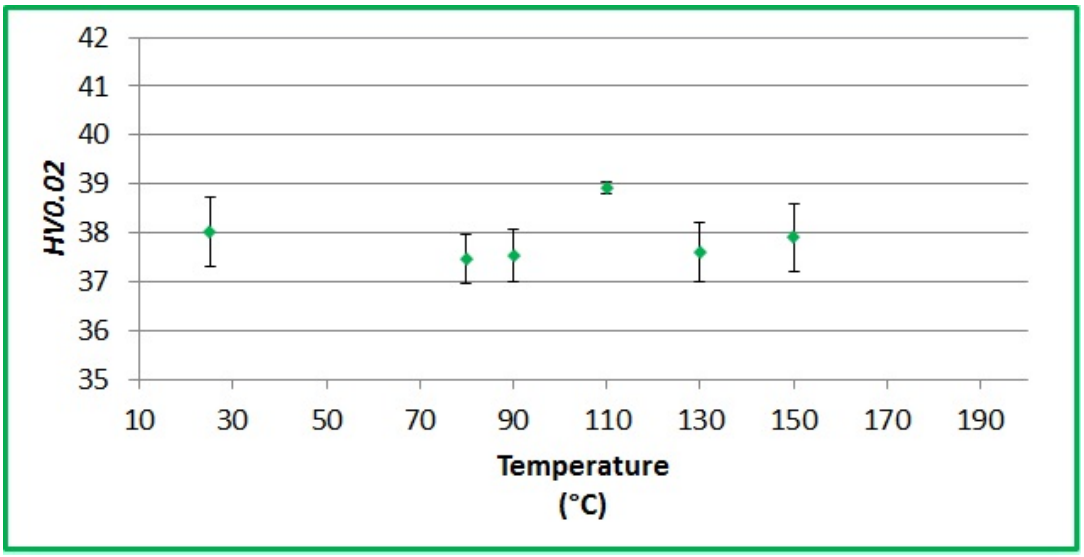

Figure 5.8: Isochronal hardness curve as a function of temperature (aging time: 10min) for XHP–Mg HPT–processed by $\gamma \approx 50$; error bars indicate $\mathbf{\Delta_{HV}}$

Name	**Aging**	$\overline{\mathbf{HV0.02}}$	$\mathbf{s_{HV}}$	$\mathbf{u_{HV}}$
070414_Mg_HPT1	none	39,4	2	0,6
080414_Mg_HPT2	none	37	1,9	0,6
070714_Mg_HPT25	none	37,5	1,8	0,6
090514_Mg_HPT16_80C_10	10min at 80°C	38,4	1,9	0,6
180914_Mg_HPT31_80C_10	10min at 80°C	36,8	2,1	0,6
180914_Mg_HPT32_80C_10	10min at 80°C	37,1	2,6	0,7
290414_Mg_HPT12_90C_10	10min at 90°C	42,6	4,9	1,1
070514_Mg_HPT14_90C_10	10min at 90°C	38,3	2,3	0,5
210514_Mg_HPT22_90C_10	10min at 90°C	36,6	1,6	0,4
210514_Mg_HPT23_90C_10	10min at 90°C	37,5	2,8	0,6
280414_Mg_HPT11_110C_10	10min at 110°C	38,9	2,5	0,6
180914_Mg_HPT29_110C_10	10min at 110°C	39,1	3,3	0,9
260215_Mg_HPT37_110C_10	10min at 110°C	38,9	2,5	0,6
260215_Mg_HPT38_110C_10	10min at 110°C	38,6	2	0,4
230414_Mg_HPT10_130C_10	10min at 130°C	38,7	2,9	0,6
290814_Mg_HPT26_130C_10	10min at 130°C	36,9	2,0	0,5
230414_Mg_HPT10_150C_10	10min at 150°C	36,0	3,0	0,9
180914_Mg_HPT30_150C_10	10min at 150°C	38,7	4,0	1,0
270215_Mg_HPT39_150C_10	10min at 150°C	37,6	2,9	0,6
270215_Mg_HPT40_150C_10	10min at 150°C	39,3	2,8	0,7

Table 5.7: Individual results of the Vickers hardness test for XHP–Mg HPT–processed by $\gamma \approx$

with the ***HV0.02*** of solely HPT–processed specimens, the ***HV0.02*** increases by $\approx 2\%$.

5.2 SEM-results

5.2.1 Untreated specimens

CP–Magnesium

Figure 5.9 shows the orientation map and the corresponding inverse pole figure (IPF) for a CP–Mg specimen as received, without any other treatment than necessary to obtain EBSD pictures.
The specimen shows a nonuniform grain-radius of $0,91\mu m \pm 1,8\mu m$ and a not to strongly developed texture in basal direction when observed in rod direction.

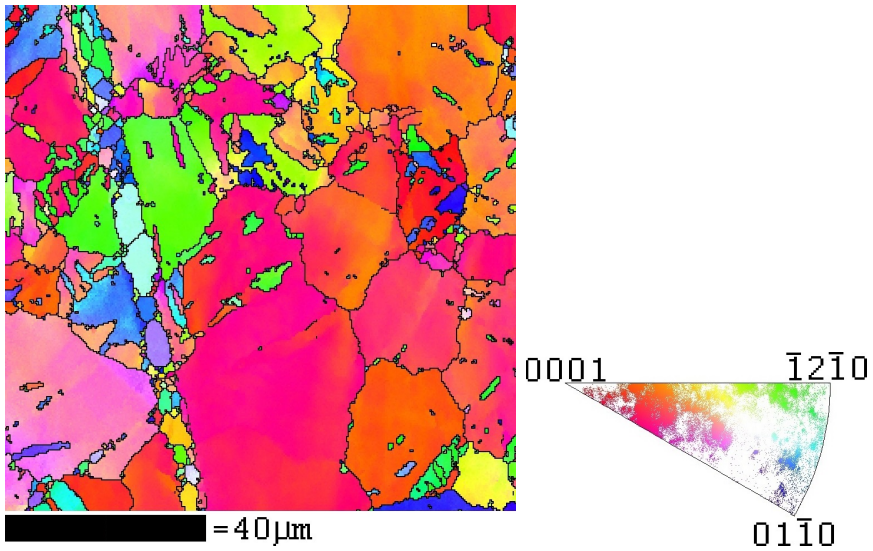

Figure 5.9: Orientation map of CP–Mg, as received from AlfaAesar

Magnesium–Zinc–Calcium

Figure 5.10 shows the orientation map and the corresponding IPF for an Mg-Zn-Ca specimen as received, without any other treatment than necessary to obtain EBSD pictures.
For the most part of figure 5.10 it was not possible to determine definite grains, but the parts where it was possible, an average radius of $0,665\mu m \pm 0,477\mu m$ was calculated. A medium developed texture in $\langle 01\bar{1}0 \rangle$ direction was determined when observed in rod direction.

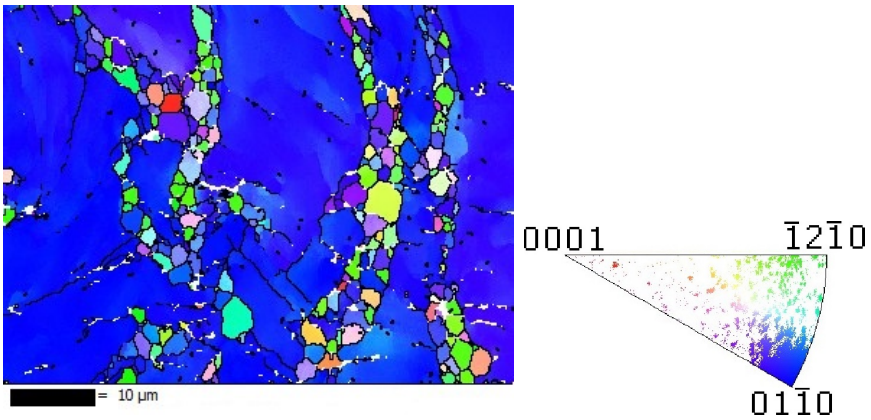

Figure 5.10: Orientation map of untreated Mg–Zn–Ca

5.2.2 Quenched Specimens

CP–Magnesium

Figure 5.11 shows the orientation map and the corresponding IPF of the specimen *190814-99.95-550q*, which was quenched from 550° C. The investigated specimen showed slight traces of oxidation after quenching and therefore was not considered as a valid data point in the series of measurement.
The grains in the specimen have a mean radius of $82\mu m \pm 61\mu m$ and show a not to strongly developed texture in the directions $\langle 01\bar{1}0 \rangle$ and $\langle \bar{1}2\bar{1}0 \rangle$ when observed in rod direction.

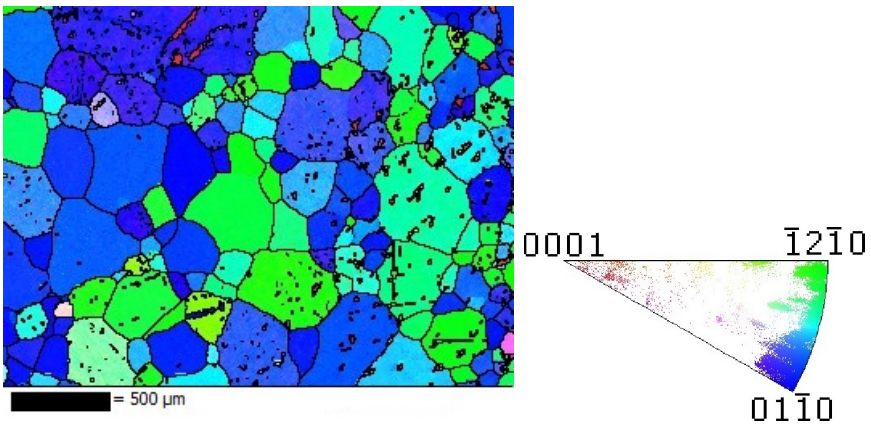

Figure 5.11: Orientation map of CP–Mg after quenching from 550°C

Magnesium–Zinc

Figure 5.12 shows the orientation map and the corresponding IPF for the specimen *201114-MgZn-550q* after quenching from 550° C. The grains have a mean radius of $216\mu m \pm 147\mu m$, show no preferred orientation and a high density of twins.

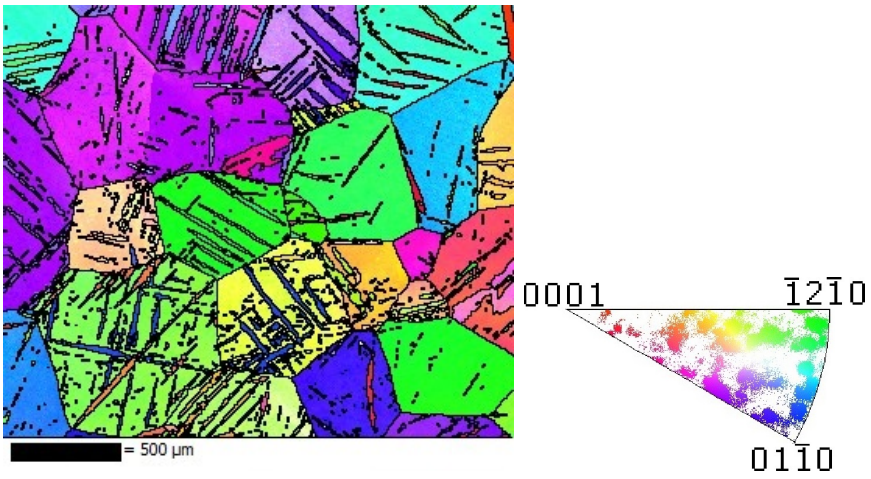

Figure 5.12: Orientation map of the Mg–Zn alloy after quenching from 550°C

Figure 5.13 shows the orientation map and the corresponding IPF for the specimen *051214-MgZn-550cd-I* after cooling the specimen in Argon atmosphere from 550°C to room-temperature over the duration of four hours. A clear texture is not discernible the density of twins is very high.

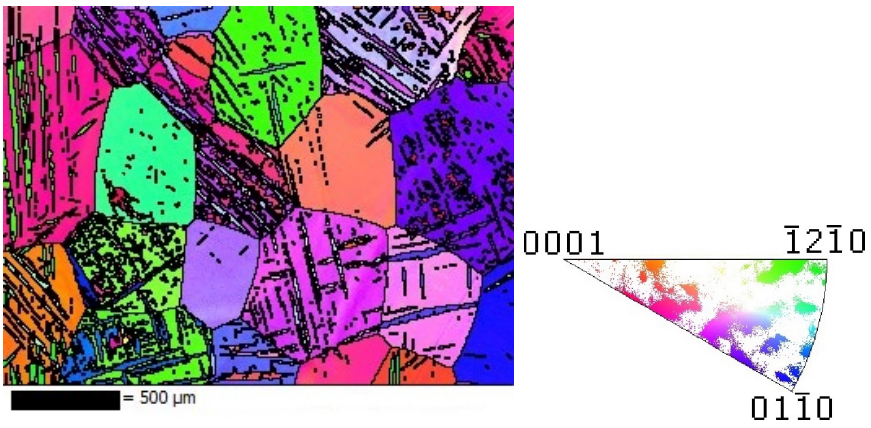

Figure 5.13: Orientation map of Mg-Zn after slowly cooling from 550°C

Magnesium–Zinc–Calcium

Figure 5.14 shows the orientation map and the corresponding IPF for the specimen *020615-MgZnCa-550q-1* after quenching 550° C. The grains have a mean radius of $70\mu m \pm 45\mu m$ and shows no clearly discernible texture when observed normal to the rod direction.

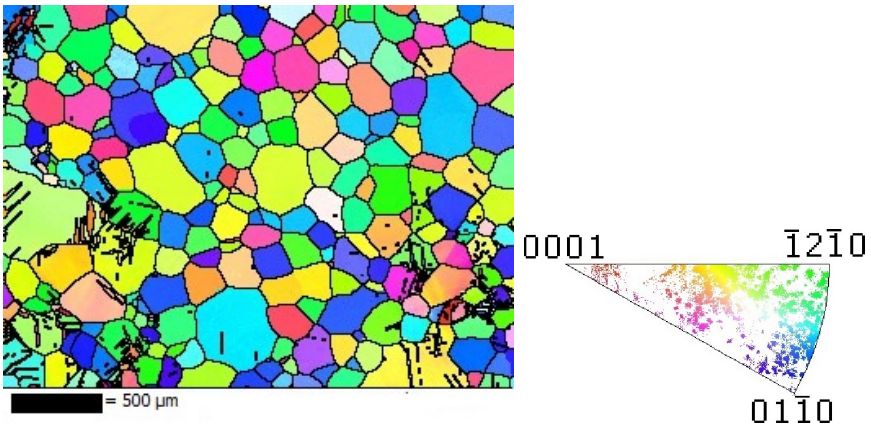

Figure 5.14: Orientation map of the Mg-Zn-Ca alloy after quenching from 550°C

5.2.3 HPT–Processed Specimens

CP–Magnesium

Figure 5.15 shows the orientation map and the corresponding IPF for the specimen *210415-99.95-HPT72* after HPT–processing at 4 GPa by 0,125 rotations. The grain-radius was calculated to be $0,96\mu m \pm 1,31\mu m$ and there is no texture apparent when observed in rod-direction.

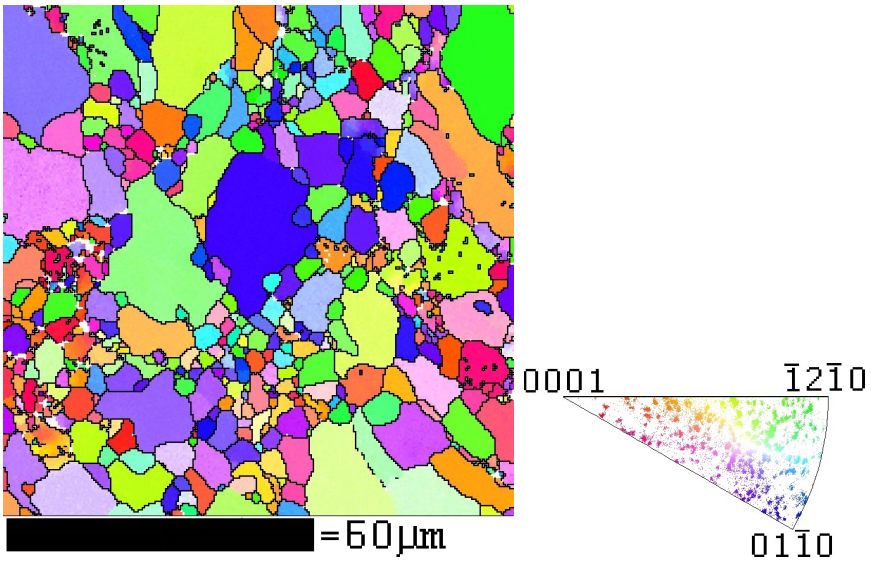

Figure 5.15: Orientation map of CP–Mg after HPT–processing by 0,125 rotations

Figure 5.16 shows the orientation map and the corresponding IPF for the specimen *061114-99.95-HPT36* after HPT–processing at 4 GPa by 2 rotations. The grain-radius was calculated to be $0,97\mu m \pm 0,80\mu m$ and a strong texture in the basal direction can be seen when observed in rod-direction.

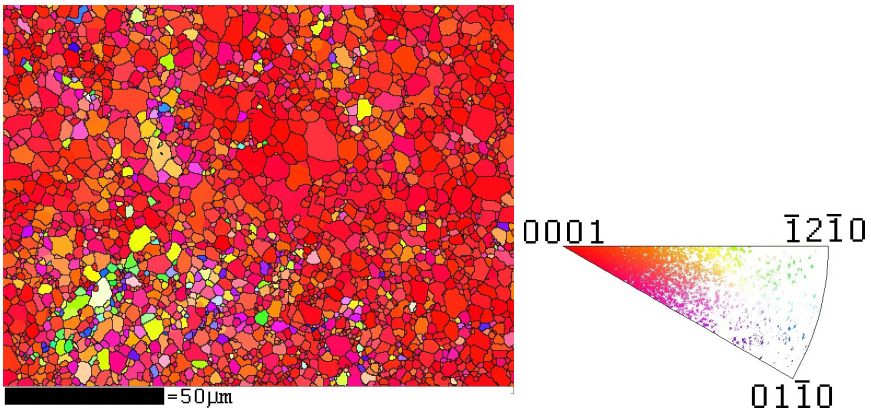

Figure 5.16: Orientation map of CP–Mg after HPT–processing by 2 rotations

Figure 5.17 shows the orientation map and the corresponding IPF for the specimen
171214-99.95-HPT54-110C-10 after HPT–processing at 4 GPa by 2 rotations and subsequent 10 min. aging at 110° C. The grain-radius was calculated to be $1,08\mu m \pm 0,94\mu m$ and a strong texture in the basal direction can be seen when observed in rod-direction.

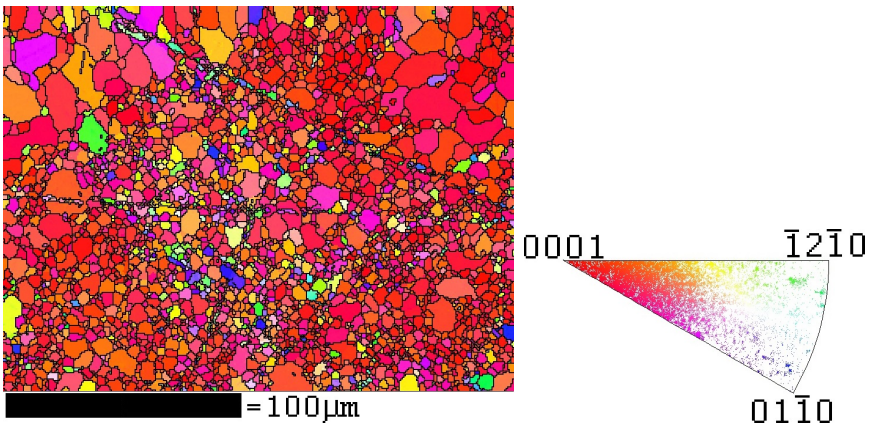

Figure 5.17: Orientation map of CP–Mg after HPT–processing by 2 rotations and 10 min. at 110°C

Figure 5.18 shows one of a series of BSE–images of the specimen *210115-99.95-HPT65-190C-10* after HPT–processing at 4 GPa by 2 rotations and subsequent 10 min. aging at 190° C. The average grain-radius was calculated from the whole series to be $4,47 \pm 2,85 \mu m$.

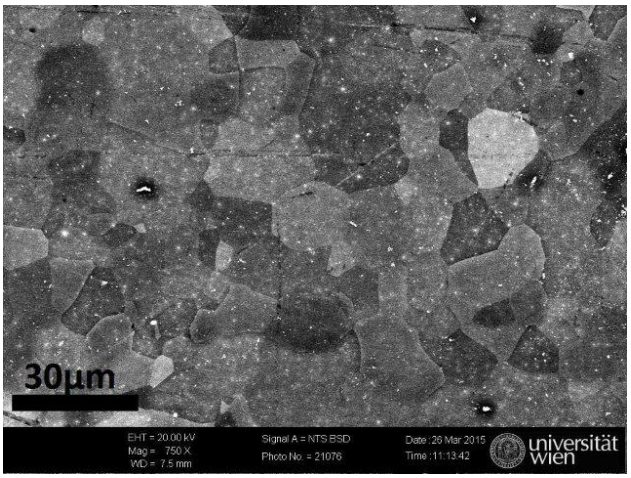

Figure 5.18: BSE image of CP–Mg after HPT–processing by 2 rotations and 10 min. at 190°C

5.3 TEM and STEM results

5.3.1 Quenched specimens

Magnesium–Zinc–Calcium

The figures 5.19a and 5.20 show typical images obtained from the specimen *051015-MgZnCa-550q-150C-10-1*, which was previously annealed at 550° C for 60 minutes, quenched and aged at 150° C for 10 minutes, in bright-field and HAADF-STEM mode, respectively.The specimen shows three different types of microsturcture:

1. **Regions without Defects:** There are regions on the specimen where almost no dislocations (5.19c) and no precipitations(

2. **Complex Dislocation Networks:** These can often be found in the vicinity of big Calcium-Oxide precipitations (lower right side of 5.19c) and show a complex structure of not only straight or bent dislocations, but also dislocation loops (5.19d)

3. **Regions with Large Precipitations:** Areas whith large precipitations are often observed in the specimen (5.20a to 5.20e . They are either Calcium-Oxide or Silicon as can be seen in 5.20c,5.20d and 5.20e, respectively. Often they are surrounded by complex networks of dislocations (5.19b, but not necessarily so (5.19a.

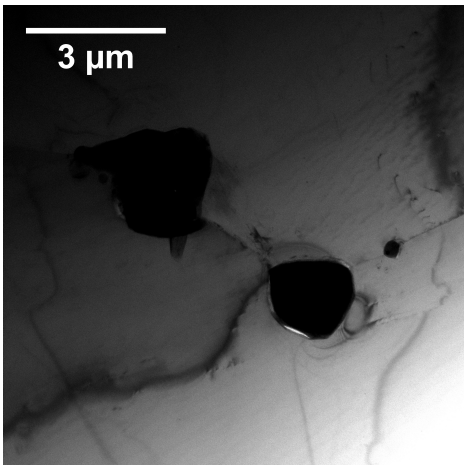

(a)

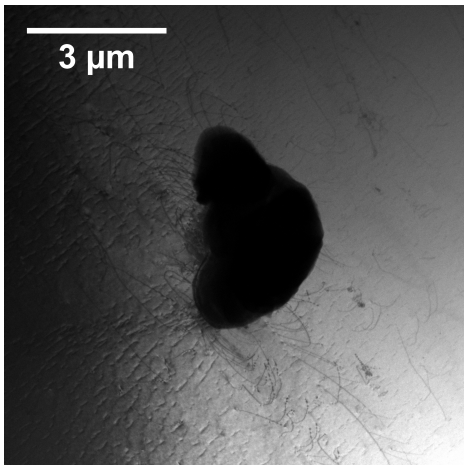

(b)

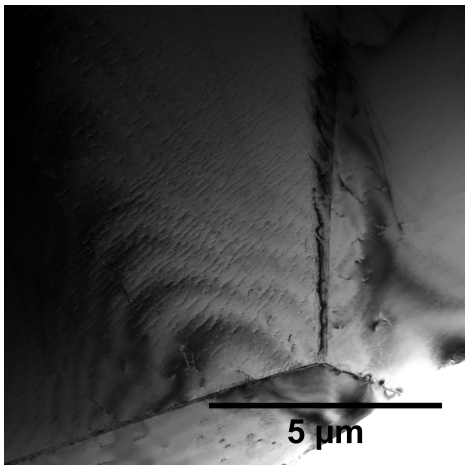

(c)

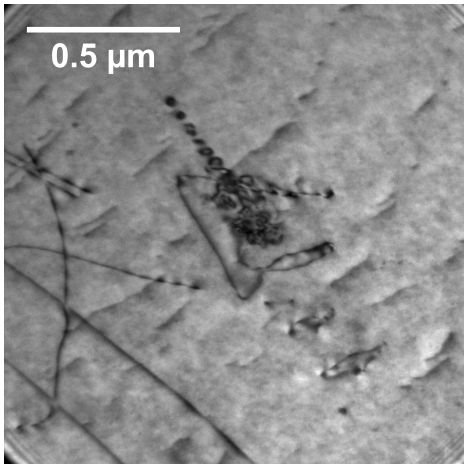

(d)

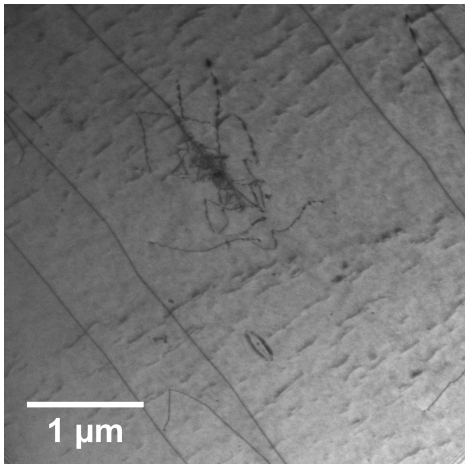

(e)

Figure 5.19: Bright field images of the Mg–Zn–Ca after quenching from 550°C and subsequent 10 min. aging at 150°

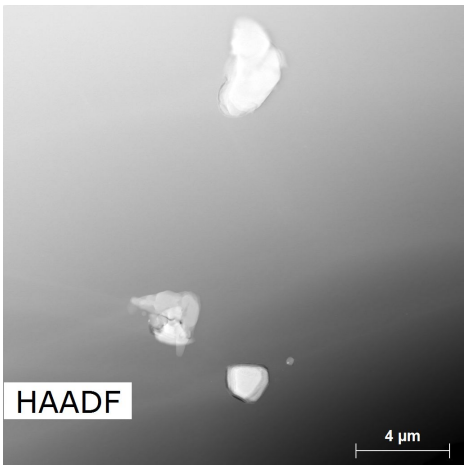

(a)

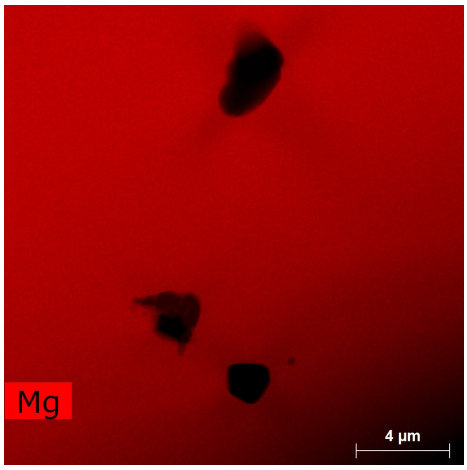

(b)

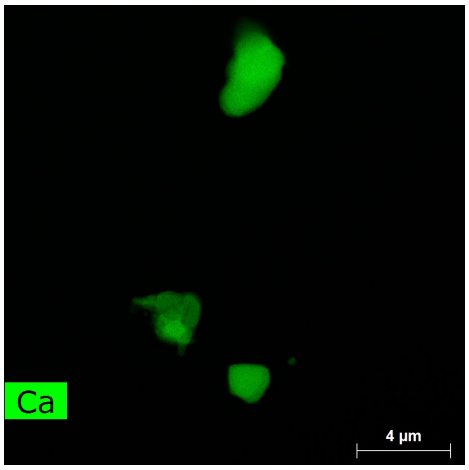

(c)

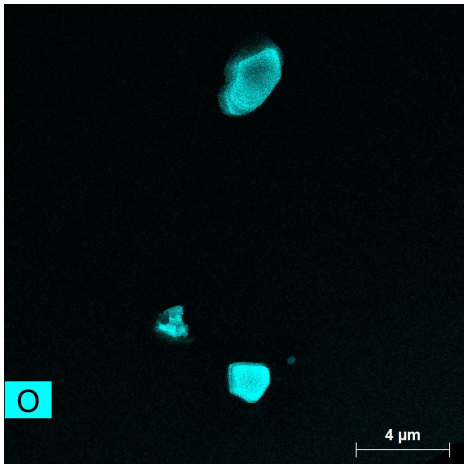

(d)

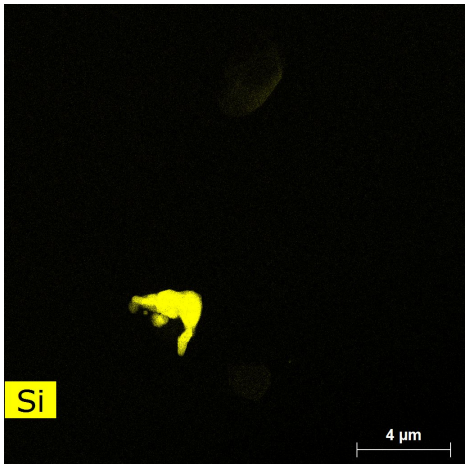

(e)

Figure 5.20: Element distribution in from 550°C quenched and at 150° C aged Mg–Zn–Ca

5.3.2 HPT processed specimens

CP–Magnesium

HPT processed CP–Magnesium) Figure 5.21 shows bright-field images of the specimen *071015-99.95-HPT83*, which was previously HPT processed at 4 GPa by 2 rotations. The grain structure is nonuniform and areas with large grains separated by areas with smaller grains can be seen (5.21a). Inside the grains, many dislocations in various forms such as straight and bent lines as well as loops, can be observed (5.21b and (5.21c)).

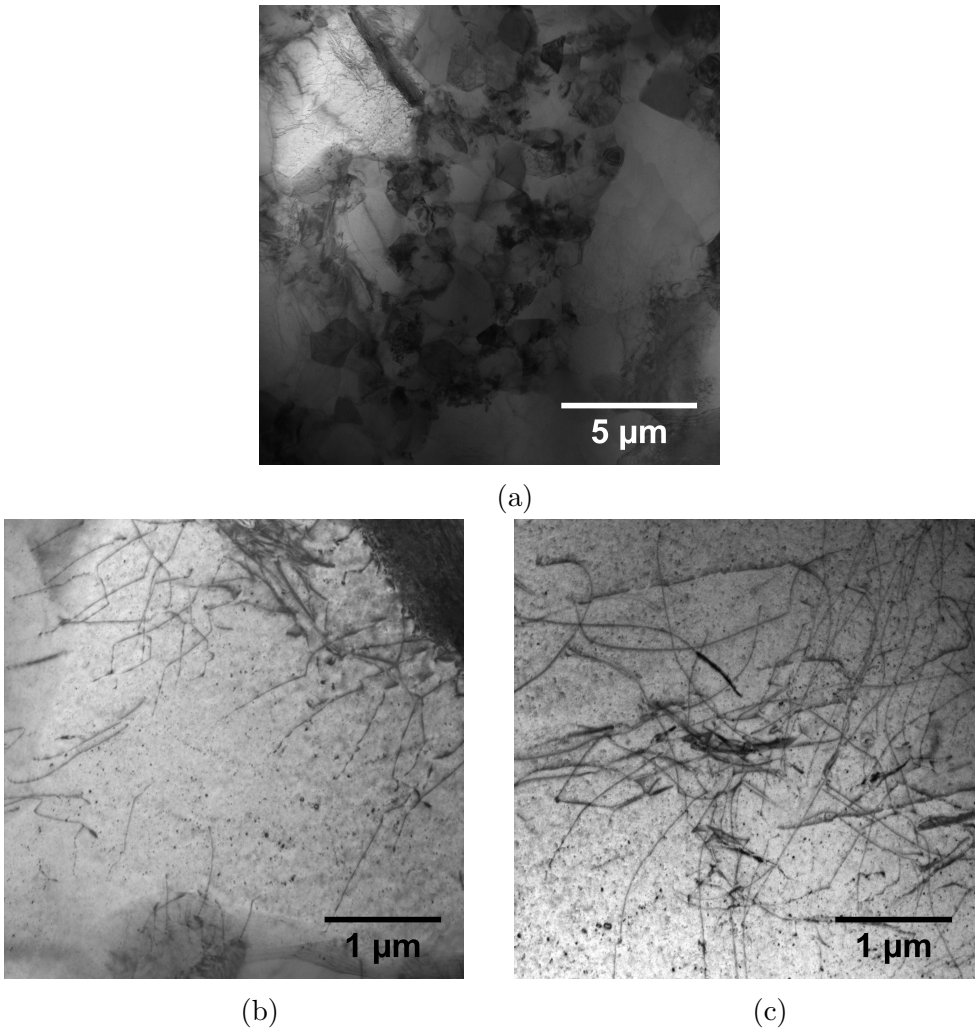

(a)

(b) (c)

Figure 5.21: Bright field images of CP–Mg after HPT–processing by 2 rotations

HPT–Processed and Aged CP–Magnesium Figure 5.21 shows bright-field images of the specimen *151015-99.95-HPT94-90C-10*, which was previously at 4 GPa HPT processed by 2 rotations and subsequently aged for 10 minutes at 90° C. The grains visible are bigger and more regular than in specimen *071015-99.95-HPT83* (see 5.3.2), but still show a high density of defects (5.22b). Especially a

high density of dislocation loops of various sizes is visible (5.22c).

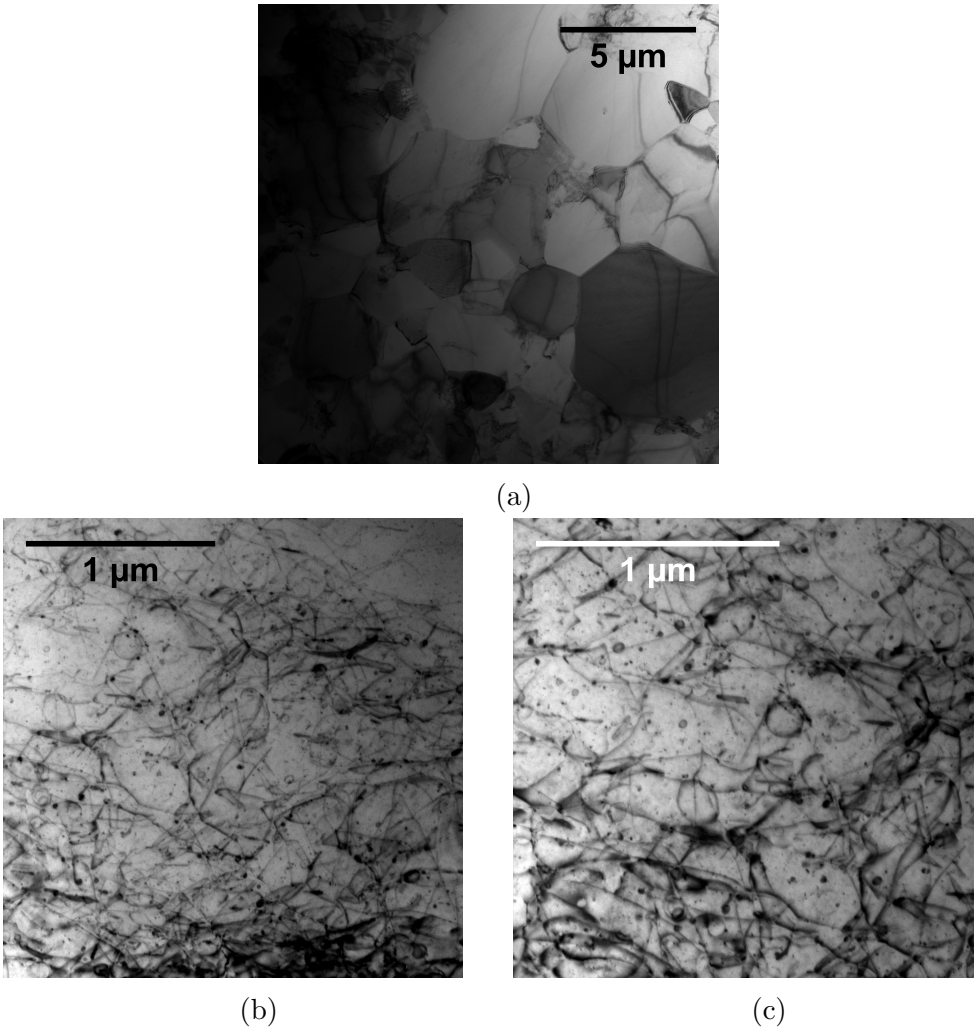

(a)

(b) (c)

Figure 5.22: Bright field images of CP–Mg after HPT–processing by 2 rotations and aging 10 min. at 90°C

Magnesium–Zinc–Calcium

HPT-Deformed MgZnCa Figures 5.23 and 5.24 show the results of TEM and HAADF-STEM investigations of specimen *091015-MgZnCa-HPT1* ($74\overline{HV}0.02$), respectively. The structure is characterized by fine grains and a high concentration of defects, which makes it difficult to identify single types of defects 5.23. Furthermore, Calcium-rich precipitations could be detected via HAADF-STEM as can be seen in figure 5.24, in which a total of 614 precipitations could be counted. They are of mostly elliptical shape and show a preferred orientation to the left upper corner of the image,but otherwise are randomly distributed.

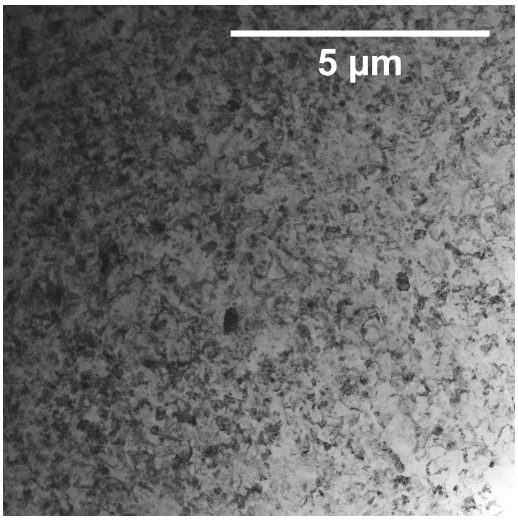

Figure 5.23: Bright field images of Mg–Zn–Ca after HPT–processing by 2 rotations

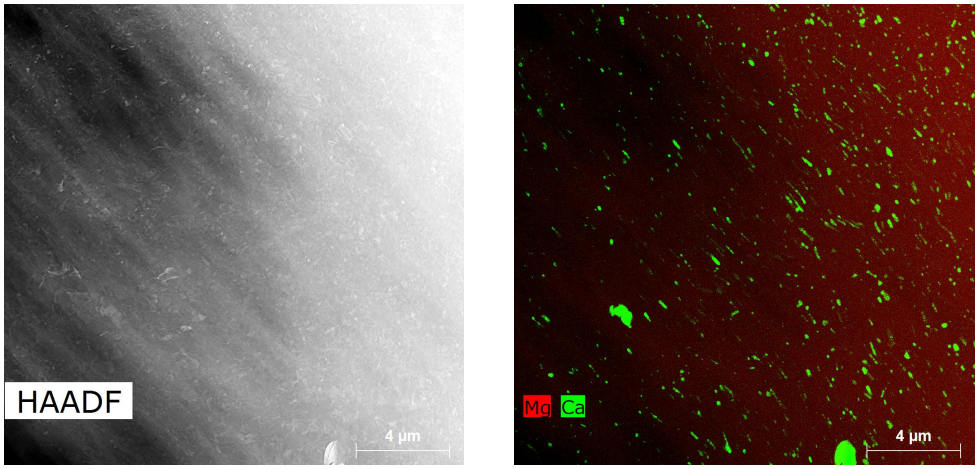

(a) (b)

Figure 5.24: HAADF image and elemental distribution of Mg–Zn–Ca after HPT–processing by 2 rotations

HPT–Processed and Aged Magnesium–Zinc–Calcium Figures 5.25 and 5.27 show bright-field and HAADF-STEM images of the specimen *141015-MgZnCa-HPT11-150C-10* $(104\overline{HV}0.02)$, respectively. The grain structure is not as fine as in the specimen 5.23 (compare 5.23 to 5.25a), but still shows a high density of defects. Furthermore, precipitations and other impurities could be detected via HAADF-STEM. Figure 5.24b shows a typical area where many (1067) small Calcium-rich precipitates can be observed. They are of either a round or elliptical shape and show no preferred direction.

In Figures 5.27a to 5.27e the HAADF–STEM images of large impurities are depicted. These consist of Calcium-Oxide (5.27c and 5.27d) or Silicon 5.27e.

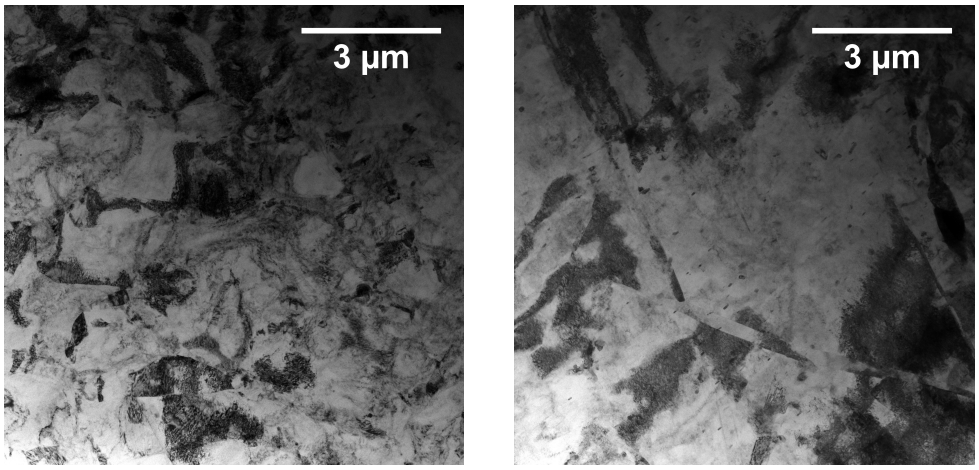

(a) (b)

Figure 5.25: Bright field images of Mg–Zn–Ca after HPT processing with 2 rotations and aging for 10 min. at 150°C

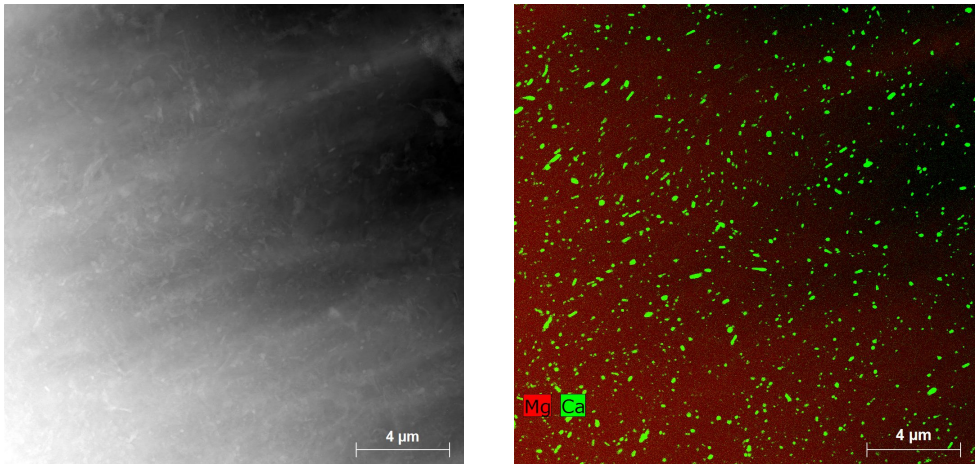

(a) (b)

Figure 5.26: HAADF image and elemental distribution of the Mg–Zn–Ca after HPT–processing by 2 rotations and aging for 10 min. at 150°C

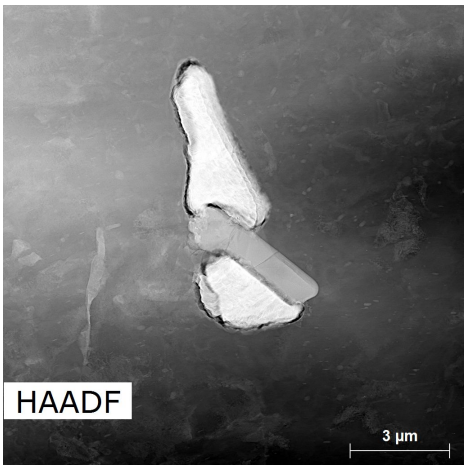

(a)

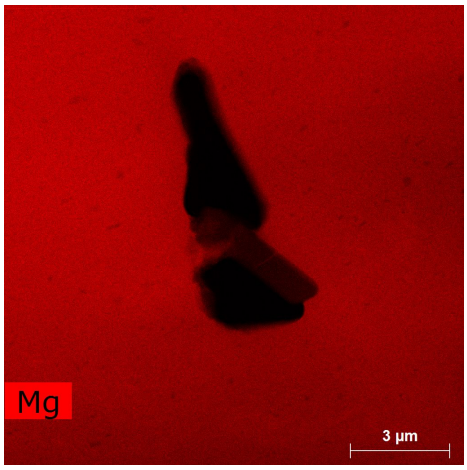

(b)

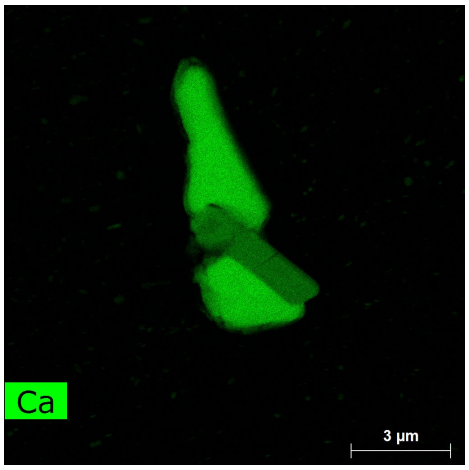

(c)

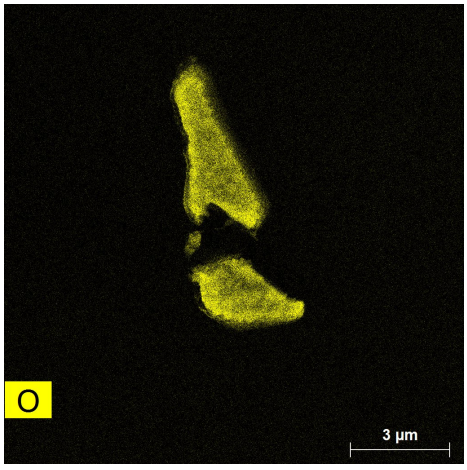

(d)

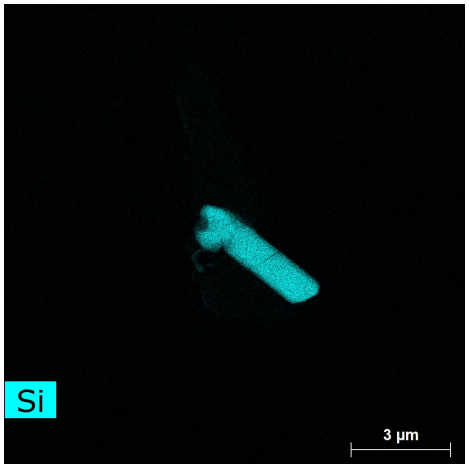

(e)

Figure 5.27: HAADF image and elemental distribution of Mg–Zn–Ca after HPT–processing by 2 rotations and aging 10 min. at 150°C

Chapter 6

Discussion

6.1 Discussion

The results given in chapter 5 are discussed here individually for each material, a comparison of the different materials will be given in chapter 7. Figures 6.1 and 6.2 provide an overview of the observed evolution of the Vickers hardness HV of quenched/aged as well as HPT–processed/aged specimens.

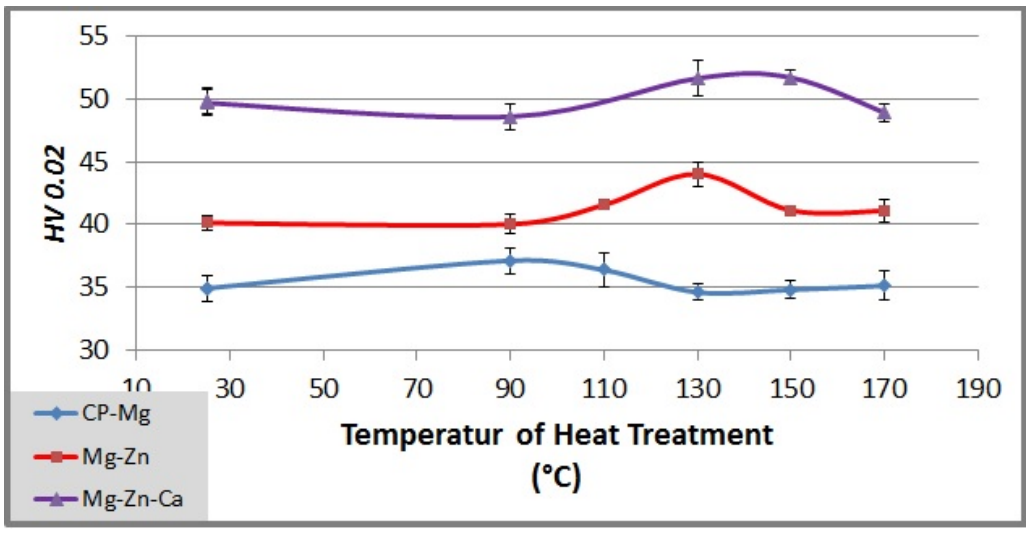

Figure 6.1: Comparison of the HV of quenched/aged specimens.

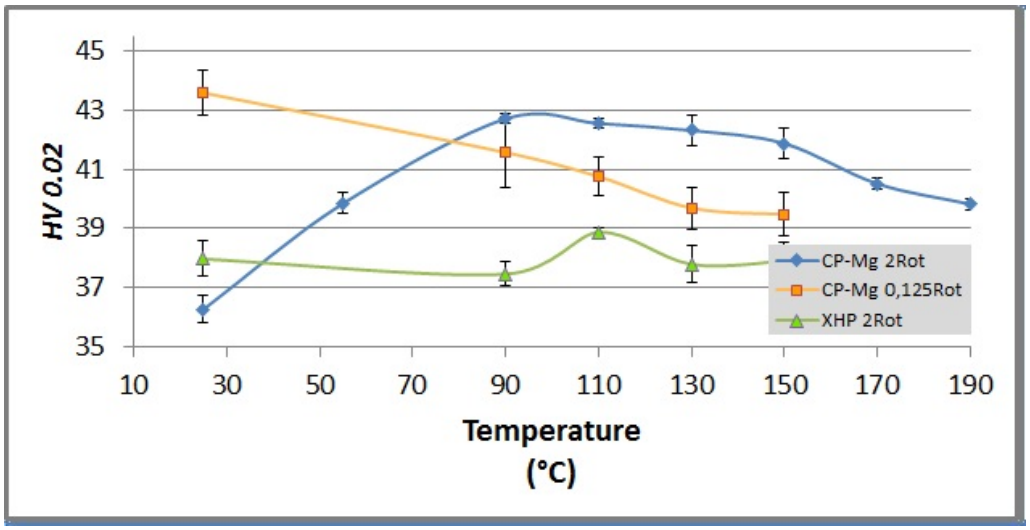

Figure 6.2: Comparison of the HV of HPT–processed/aged specimens.

6.1.1 CP–Magnesium

Quenched CP–Magnesium

First of all, an inspection of the results (compare figure 5.1 to figure 5.2) of quenched specimens suggests that there is an influence of oxidation. Indeed, if only sand-blasted or ground with rough grinding paper, specimens always show visual traces of oxidation.

The oxidized specimens show a initial HV level of $\boldsymbol{HV0.02} \approx 45$, and achieve their maximum HV of $\boldsymbol{HV0.02} \approx 50,5$ in the course of aging at 170°C. The non–oxidized specimens show a initial HV level of $\boldsymbol{HV0.02} \approx 35$, and achieve their maximum HV of $\boldsymbol{HV0.02} \approx 38$ in the course of aging at 90°C. Comparing the results presented in this work to results reported by Hampshire and Hardie [13] two observations are apparent:

1. Hampshire and Hardie report that the maximum 0.1% flow stress is measured after aging "at about 160°C" and "decreases for aging temperatures above 170°C" [13] while in the presented work the maximum HV is measured after aging th quenched specimens at 90°C for non–oxidized specimens and at 170°C for oxidized specimens (see 5.1.1).

2. In case of Hampshire and Hardie [13], the maximum increase in 0.1% flow stress is $\approx 60\%$ after aging compared to the solely quenched specimens, while in the present work the maximum increase in HV is $\approx 12\%$ for specimens that oxidized during quenching, and $\approx 6\%$ for non–oxidized specimens after aging compared to solely quenched specimens.

To address these points, consider that the results reported by Hampshire and Hardie [13] may be contaminated by Magnesium–Oxide (MgO) and the consequences of such a contamination. The motivation for this consideration stems from figure 1.3: In this figure, not only quenched–in dislocation loops, to which the authors [13] attribute the hardening effect are shown, but also other complex dislocation structures, which the authors attribute to a general "strain". Hampshire and Hardie describe their experimental procedure as follows:

"Magnesium of 99.95% purity was melted under flux and sprinkled with sulphur during pouring to keep oxidation to a minimum. The cast material was extruded at 360°C to 4,75 mm diameter rod and then cold-drawn to 4,32 mm wire.....Heat treatment before quenching was accomplished in a sealed furnace which had a few percent of sulphur dioxide added to its atmosphere to promote formation of a protective coating on the specimens and so combat more extensive oxidation." [13]

While it can be argued that pure sulfur melts at 115°C and starts boiling at 445°C [47], and therefore will not be present in the material during quenching from 575°C, the reaction of Magnesium and Sulfur-dioxide at high temperatures (especially in even slightly wet atmospheres) is known [48].

$$2Mg(s) + SO_2(g) \longrightarrow 2MgO(s) + S(s) \tag{6.1}$$

Furthermore, the authors don't deny the possibility that oxidation occurs, but do not consider the effects it might have on the material.
If one assumes that a large MgO particle is formed before or during the heat treatment before quenching, the effect a rapid cooling can have on the Mg matrix can be calculated using the approach presented by Hull and Bacon [12].
The change in length Δl of a material with the original length l_0 that experienced the temperature change ΔT can be estimated to be

$$l_1 = l_0(1 + \Delta T) \tag{6.2a}$$
$$\Delta l = l_0 \alpha_L \Delta T \tag{6.2b}$$

with α_L as the material specific linear expansion coefficient.
Consider the quenching ΔT of a (comparatively soft) matrix with a hole of radius r^h in which a stiff inclusion with a radius r^i sits. Heating the material and keeping it at a constant temperature T_q will lead to a relaxation of the matrix around the

inclusion. Rapidly changing the temperature to T_{RT} will lead to a change in the inclusion and hole radius according to equation 6.2:

$$r_1^i = r_0(1 - \alpha_i \Delta T) \tag{6.3a}$$

$$r_1^h = r_0(1 - \alpha_h \Delta T) \tag{6.3b}$$

The resulting misfit ϵ, which causes a displacement u_r of the matrix, can be calculated to be

$$\epsilon \equiv \frac{r_1^i - r_1^h}{r_1^h} = \frac{r_0 \Delta T(\alpha_h - \alpha_i)}{r_0(1 - \alpha_h \Delta T)} \tag{6.4}$$

The displacement of the matrix u_r is purely radial and results in a strain field of pure shear, which is maximal at the interface of the inclusion and the matrix and on a cylinder surrounding the inclusion with a diameter of $\sqrt{2}r_1$ [12]. The corresponding maximum shear stress is

$$\tau_{max} = 3\,\epsilon\,G_M \tag{6.5}$$

with G_M as the shear modulus of the matrix. If τ_{max} is bigger than the Peierls stress τ_p of Mg, dislocations can nucleate. Calculating the τ_{max} of an inclusion with the parameters given in table 6.1, it can be shown that a MgO particle induces sufficient stress if immediate cooling is assumed.

Parameter	value	source
G (Mg)	17,3 GPa	[22]
α (Mg)	$26 \cdot 10^{-6} K^{-1}$	[1]
α (MgO)	$11 - 13, \cdot 10^{-6} K^{-1}$	[49]
α (CaO)	$15,2 \cdot 10^{-6} K^{-1}$	[49]
Δ T	525 K	
τ_p (basal)	0,52 MPa	[50]
τ_{max} (CaO)	$\approx$ 300 MPa	6.5
τ_{max} (MgO)	$\approx$ 380 MPa	6.5

Table 6.1: Coefficients of thermal expansion, Δ T, τ_{max} and τ_p

MgO particles, together with the dislocations surrounding them, give a good explanation for the higher initial HV of the oxidized CP–Mg specimens. They might also provide an explanation for the – compared to the non–oxidized specimens – higher aging temperature to achieve maximum HV:
The recovery and recrystallization of vacancies and vacancy type dislocations as well as the quenched-in dislocations is hindered by the MgO particles.

A similar effect is observed in the investigated the Mg–Zn–Ca specimen, where a large Calcium–Oxide particle is surrounded by dislocations (see 5.19b).

HPT–processed CP–Magnesium

In case of HPT–processing treatment, three characteristics of figure 5.6 are to be pointed out:

1. The initial HV of specimens being HPT–processed by $\gamma \approx 50$ ("strongly deformed specimens") is lower than the initial HV of specimens HPT–processed by $\gamma \approx 3$ ("weakly deformed specimens").

2. The strongly deformed specimens show an increase in HV with aging, whereas the weakly deformed specimens soften.

3. The aging temperature needed to achieve the maximum HV in the strongly deformed specimens matches the aging temperature needed to achieve the maximum HV in the quenched specimens.

Comparing the isochronal HV curve of strongly deformed CP–Mg (figure 5.7) with the isochronal HV curve of quenched CP–Mg (figure 5.1) a significant drop in HV can be recognized at $\approx 130°$ C in the first case, whereas in the second case the HV does not change significantly until aging at 170° C [1] .
The fact that the strongly deformed specimens are softer than the weakly deformed specimens might be caused by either dynamic/static recrystallization (work softening) or by a texture effect. The effect is not caused by a Hall-Petch effect, because the grains in the weakly deformed specimens are larger (figure 5.15). XRD–profile analysis [2] show a slightly lower dislocation density in the strongly deformed specimens, which can not account for the decrease in HV observed. In the histogram of a weakly deformed specimen (figure 5.5), two different peaks are visible, one at $\approx$ HV0.02 = 38 and one at $\approx$ HV0.02 = 45 of which the first one obviously corresponds to the recrystallized i.e. soft parts of the material and the second one to the strongly deformed, but not yet recrystallized sample. The author therefore proposes that dynamicstatic recrystallization in CP–Mg starts at shear stains smaller than $\gamma \approx 3$.

Another noticeable effect is the increase in HV of the strongly deformed specimens when aged. This increase in HV is **not** due to changes of grain size or dislocation density, texture effects, twinning or precipitations: The grain size does not

[1] compare to the results of [13] who also observe a drop in flow stress after aging at temperatures higher than 170° C

[2] in cooperation with E.Schafler

change significantly after aging (compare to chapter 5.2.3), XRD–profile analysis [2] show a lower dislocation density in aged specimens and neither texture changes nor precipitations could be identified (see chapter 5.2). The effect is strongest at 90° C and statistically significant.
The explanation for this effect may be found in the bright-field TEM images 5.21 and 5.22. They show dislocation loops, in both cases in varying sizes, but generally smaller ones in the first case and bigger ones in the second case. Both specimens were prepared for TEM investigation in the same manner (see chapter 3.2.5), therefore this effect is not caused by preparation. The obvious growth or even the formation of new vacancy-type dislocation loops can only be due to the presence and migration of vacancies, as prismatic loops cannot expand through conservative dislocation glide [12]. A similar effect was observed in the work by Xiaoxu et al.[53] in accumulatively roll bonded (ARB) Aluminium of 99.2% purity which afterward was aged for 30 minutes at 150° C. The authors describe an increase by ≈ 8,5% in yield strength but also a loss of ductility after aging, and attribute this to the loss of dislocation sources during aging. This leads to the activation of new dislocation sources during re-straining which requires a marked increase of stress.
Comparing the results of [53] to the results at hand, it is unlikely that the observed effect stems from similar dynamics, for the following reasons:

1. Different aging times: for the work at hand the specimens were aged for 10 minutes at 90° while in [53] the specimens were aged for 30 minutes at 150° C, thus making annealing of dislocation more probable.

2. Different microstructures: The smallest distances between grain boundaries reported by [53] are in the range of 180 nm before and 225 nm after aging, while HPT–processed Mg of this work shows a wide grain size distribution around 1 μm before and after aging at 90° C.

Especially the last point was investigated by Renk et al.[54], who found that grain sizes below a material specific critical grain size, typically in the range of 300 nm, are necessary for this effect to happen.
In the aging range of 90°C to 150°C a slight downward trend in HV may be assumed from figure 5.7 while only in the course of aging at 170°C a significant drop in HV is observed. Grain sizes were determined to be ≈ 4,5 μm for at 190°C aged Mg which leads to the conclusion that recrystallization starts from temperatures larger than 150°C .

Finally, let us compare now the hardening effects in quenched/aged and HPT-processed/aged specimens of CP–Mg: It can be concluded that beyond a critical processing strain, HPT–processed CP-Mg specimens show an increase by 9% to

17% in HV in the course of aging during a temperature range from 55°C and 150°C. The quenched and subsequently aged specimens show an increase by ≈ 6% in HV, and at a distinct temperature of 90°C, which falls into the temperature range of the maximum occurring with the HPT–processed specimens. This finding clearly supports the hypothesis that the presence and coarsening of vacancy–type dislocation loops is responsible for the observed hardening effects not only in quenched but also in HPT–processed CP–Mg.

6.1.2 XHP–Magnesium

The most noticeable feature in figure 5.8 is the – compared to CP–Mg – very pronounced maximum. The maximum HV occurs in the course of aging of HPT–processed specimens at 110° C, with a significant increase by ≈ 2% . This effect is not as large as in CP–Mg, which leads to the conclusion that even a very small amount of impurities can change the properties of a material significantly. A significant drop in HV in the course of aging HPT–processed specimens at 130° C can also be observed, whereas in CP–Mg a marked decrease in HV occurs in the course of aging HPT–processed specimens at 170° C. It is therefore very likely that recovery and recrystallization in XHP–Mg happen at lower deformations than in CP–Mg, as the defects annihilate easier because of the lack of impurities. All this might contribute to the hardening effect and therefore further investigations are strongly encouraged.

6.1.3 Magnesium–Zinc

Concerning quenched Mg–Zn specimens, they show the largest increase in HV of all investigated materials in the course of aging. The maximum HV – with a gain of ≈ 9% compared to the solely quenched specimens – is measured after the aging of the quenched specimens at 130° C. Aging at other temperatures does not lead to a significant increase in HV (see figure 5.3).
The most striking feature in the Mg–Zn specimens is the high density of twins. These twins are found in approximately equal densities in quenched (figure 5.12) as well as in slowly cooled (figure 5.12) specimens, which suggests that the twins are formed during the grain growth which occurs during heating of the specimens.
Since the specimen are kept at 550°C for 60 minutes it is unlikely that more twins form during the aging treatment after quenching, which suggests that the twins are not the reason for the increase in HV at 130°C.
The specimens in question have not been specifically analyzed with respect to precipitations, since Zinc added in quantities less than 6,2wt% is soluble in Magnesium [28]. Because neither large nor small non-coherent particles with a significant Zinc

content have been found in the Mg–Zn–Ca specimens, this suggests that such particles are also not likely to be formed in Mg–Zn and therefore the mechanism of precipitation–hardening seems to be unlikely to occur, too.
Compared to the quenched CP–Mg, Mg–Zn specimens show a larger increase in HV (by $\approx$ 9%), which also occurs at higher aging temperatures. This suggests that the Zn atoms act as trapping sites for vacancies [25], not only leading to an increase of vacancy concentration in the specimens but also restricting the mobility of quenched-in vacancies to form larger agglomerates or dislocation loops, thus explaining the temperature shift of the maximum HV.

6.1.4 Magnesium–Zinc–Calcium

The marked feature of Mg–Zn–Ca are the large Calcium-Oxide (CaO) particles, which can be equally found in non-treated, HPT–processed and quenched specimens. Also Silicon particles are present and always located close to the CaO particles. It can be concluded that the CaO is formed during casting of the alloy, and that the silicon particles got stuck on them during the grinding process, as the grinding paper contains SiC_4 particles. These particles are considerably harder than Magnesium and its metallic alloys, and typically have a diameter of $\approx 2\mu m$.

Quenched Mg–Zn–Ca Quenched Mg–Zn–Ca specimens show an increase in HV by $\approx$ 5% in the course of aging at 130° C and 150°C, respectively. Compared to the results reported by Horky et.al. ([9][10]) (see figure 1.1), it can be seen that the aging temperatures needed to achieve the maximum HV do coincide.
Since an increase in HV in the course of aging of the quenched specimens occurs at 130° C which is the same temperature as in Mg–Zn specimens, this suggests that the same process of trapping vacancies by Zn is responsible for the HV increase in Mg–Zn–Ca in the course of aging at 130° C.
In order to explain the increase in HV in the course of aging of quenched Mg–Zn–Ca at 150° C, corresponding STEM investigations were undertaken (see chapter 5.3.1). Figure 5.19b shows that large Calcium-Oxide inclusions in the specimen are surrounded by complex dislocation networks,and also bowed dislocations can be seen. This supports the hypothesis presented in 6.1.1: the dislocations originate from different thermal expansions of pure Magnesium and CaO, respectively (compare to table 6.1). Furthermore, the CaO particles and dislocations surrounding them may impede the recovery and recrystallization of vacancy–type dislocations, similarly as the MgO particles do in CP–Mg.

HPT–Processed Mg–Zn–Ca. To investigate the results of Horky et al. ([9][10]) more closely, two Mg–Zn–Ca specimens, HPT–processed and aged at 150°C. The increase in HV in the course of aging compared to the solely HPT–processed specimen was $\approx$ 37 %, which is in accordance with the values reported by Horky at.al ([9][10]).

Furthermore, these specimens were investigated in a STEM (see chapter5.3.2). The solely HPT–processed specimen shows a considerable amount of small Calcium-rich precipitations, and the additionally aged specimen even more of them, as can be seen in figures 5.24 and 5.27. The assumption that these may increase the hardness of the material was therefore considered and evaluated using equation 2.5.

To calculate the volume fraction occupied by Mg-Ca phase, a region of equal specimen thickness of $\approx 200nm$ was selected. The thickness was determined with the help of stereopairs for the two investigated specimens (see [51] for more information).The area of each precipitation as well as the total area occupied by them in both sections was evaluated using the "ImageJ 1.47V" program. Assuming the particles to be circular in shape, the radius was calculated for each particle from its area, subsequently the mean radii μ_P^{HPT} and μ_P^{150} and related standard deviations σ_P^{HPT} and σ_P^{150}.

Equation 6.6 was used to obtain the volume fractions f^{HPT} and f^{150} occupied by the precipitations from the known area fractions f_A^{HPT} and f_A^{150}.

$$f^{HPT} = \frac{4}{3}\frac{\mu_P^{HPT} f_A^{HPT}}{h} \tag{6.6a}$$

$$f^{150} = \frac{4}{3}\frac{\mu_P^{150} f_A^{150}}{h} \tag{6.6b}$$

From these, the contribution of the Orowan stress $\Delta\sigma_y$ could be estimated following equation 2.5.

$$\Delta\sigma_y = 0,538\frac{Gb\sqrt{f}}{D} ln\left(\frac{D}{2b}\right)$$

Table 6.2 summarizes the results.

	HPT	HPT+150
HV0.02 (measured)	74	102
HV0.02 (measured)	726 MPa	1001 MPa
Volume fraction f of Ca-rich precipitates	$\approx$ 0,5%	$\approx 1,7\%$
Radius R of Calcium-rich precipitates	38 nm	58 nm
Orowan hardening $\Delta HV = 3 \cdot \Delta\sigma_y$	$\approx$ 40 MPa	$\approx$ 52 MPa

Table 6.2: Comparison of the precipitations in solely HPT–processed and additionally for 10 minutes at 150°C aged Mg–Zn–Ca

Although this estimation is rough and based on only two recorded HAADF–STEM images, the observed difference in HV before and after aging is far too large compared to the calculated one. Therefore one concludes that that Mg–Ca rich precipitations do not play an important role in hardening. Furthermore, the high concentration of defects – aside from Ca–rich precipitations – found in both the HPT–processed and additionally aged specimen should be emphasized (compare the bright–field micrographs 5.23 and 5.25 with figures 5.24 and 5.27, respectively). These defects impede the movement of dislocations, and thus Orowan–hardening from the precipitations identified seems unlikely even from this point of view. This result suits to the observations of Bamberger et al.[32] that Mg_2Ca particles show no significant hardening effect.

Chapter 7

Summary and Conclusion

7.1 Summary

7.1.1 Quenching

CP–Mg, Mg–Zn and Mg–Zn–Ca specimens were quenched from 550° C, subsequently aged for 10 minutes, and the Vickers hardness HV was determined for each specimen.

1. **Non–oxidized CP–Mg** specimens aged at 90° C after quenching showed an increase by **≈6%** in HV compared to the HV of solely quenched specimens.
2. **Mg–Zn** specimens aged at 130° C after quenching showed an increase by **≈ 9%** in HV compared to the HV of solely quenched specimens.
3. **Mg–Zn–Ca** specimens aged at 130° C and 150° C showed an increase by **≈ 5%** in HV compared to the HV of solely quenched specimens

The – on average – smallest grains were found in Mg–Zn–Ca ($\approx 70\,\mu m$) while Mg–Zn ($\approx 216\,\mu m$) showed the largest grains and a very high density of twins. Only the investigated CP–Mg specimen shows a distinct texture.
TEM investigations of a quenched and aged Mg–Zn–Ca specimen showed micrometer–sized CaO particles surrounded by complex dislocation networks and occasionally dislocation loops typical of quench hardening.
Mg–Zn showed – by ≈ 9% – the largest increase in HV of all investigated materials while Mg–Zn–Ca showed – by ≈ 5% – the least increase in HV, although both materials showed their maximum HV in a comparable temperature range (130° C to 150° C). Zn atoms may act as trapping sites for vacancies in both materials, thus shifting the aging temperature from 90° C in CP–Mg to 130° C in Mg–Zn. The significantly larger grains in Mg–Zn may enable a higher present density vacancies, whereas in Mg–Zn–Ca the density of grain boundaries, which act as sinks for vacancies, is higher

and therefore the density of vacancies is reduced. The HV of CP–Mg increases in the course of aging at 90°C by only ≈ 6%, because of the relative lack in impurities for trapping the vacancies compared to the other materials. Still, the grains are – with ≈83 μm – comparable to the grains of Mg–Zn–Ca, but smaller than the grains of Mg–Zn, thus explaining the lower increase in HV because of enhanced vacancy annihilation at the grain boundaries.

7.1.2 HPT–Processing

CP–Mg specimens were HPT–processed by 0,125 and 2 rotations, respectively, and XHP–Mg specimens by 2 rotations. Specimens of both materials were subsequently aged for 10 minutes and the Vickers hardness HV was determined for each specimen.

1. **CP–Mg** specimens HPT–processed by $\gamma \approx 3$ showed a decrease in HV in the course of aging.

2. **CP–Mg** specimens HPT–processed by $\gamma \approx 50$ showed an increase in HV in the course of aging between 90° C and 150° C with the largest increase by ≈ **17%** at 90° compared to the HV of the solely HPT–processed specimens.

3. **XHP–Mg** specimens showed an increase by ≈ **2%** in HV in the course of aging at 110° C compared to the HV of solely HPT–processed specimens.

4. **Mg–Zn–Ca** specimens HPT–processed by $\gamma \approx 50$ showed an ≈ **37%** increase in HV after aging at 150° C compared to the solely HPT—processed specimens, which is in good accordance with the results reported by Horky et al. ([9][10]).

The investigated CP–Mg specimens HPT–processed by 2 rotations showed a clear texture, which does not change with aging. TEM investigations of selected CP–Mg specimens show small dislocation loops in the solely HPT–processed specimen and dislocation loops of various sizes in the HPT–processed and additionally at 90° C aged specimen.

While in both materials, CP–Mg and Mg–Zn–Ca, the effect of hardening in the course of the aging of HPT–processed specimens could be observed, they showed the following differences:

- The absolute HV values of Mg–Zn–Ca specimens were always higher than those of CP–Mg.

- The aging temperature to achieve the maximum HV was higher in Mg–Zn–Ca (130° C – 150° C) than in CP–Mg (90° C).

- A higher increase in HV after aging was achieved in Mg–Zn–Ca (37%) compared to CP–Mg (17%).

As in the case of the quenched materials, these differences reflect the influence of alloying elements, which hinder recovery and recrystallization not only during deformation but also during aging, thus leading to higher aging temperatures to launch the migration of vacancies. The alloy atoms also act as effective trapping sites for vacancies, which explains the higher increase in HV in Mg–Zn–Ca compared to CP–Mg. STEM investigations of selected Mg–Zn–Ca specimens show an increase in Ca–rich precipitations after aging compared to the solely HPT–processed specimen, which turned out, however, to account for only $\approx$ 2% of the total aging-induced difference in HV observed.

7.2 Conclusion

In CP-Mg being HPT–processed beyond a critical strain, an unusual hardening effect of 17% after aging at 90°C was found. The aging temperature for this effect coincides exactly with the aging temperature to achieve the maximum HV after quenching. This suggests the formation of multivacancies and vacancy-type dislocation loops and their coarsening as the reason for the hardening. Multivacancies and dislocation loops form effective obstacles for deformation carrying dislocations and thus lead to the observed increases in HV. Compared to the quenched specimens, HPT–processed specimens show a larger increase in HV after aging, which is likely to arise from the higher concentration of vacancies produced by HPT–processing which can reach vacancy concentrations being close to that at the melting point [16]and much easier to be achieved than by quenching from those temperatures especially in bulk specimens used in this work. Moreover, the annihilation of vacancies induced by plastic deformation is hindered by the high hydrostatic pressure applied during HPT–processing [16].

For Mg–Zn–Ca, the aging temperatures (130° C – 150° C) needed to achieve the maximum HV–increase in quenched/aged as well as in HPT–processed/aged specimens also coincide. This effect cannot be explained with the increase of Ca–rich precipitations as none of them were observed in the quenched/aged specimens. Tough in the HPT–processed/aged specimen, additional precipitations were identified, their amount was far too small to quantitatively account for the hardening effect observed. The influence of other hardening effects, such as grain–boundary or work hardening, decreases as the temperature increases and therefore a similar effect of vacancy migration as observed in CP–Mg is proposed to explain the increase in HV.

Bibliography

[1] Mordike B, Lukac P. Physical Metallurgy. In: Friedrich H, Mordike B, editors. Magnesium technology (Vol. 788)Berlin-Heidelberg:Springer-Verlag; 2006.

[2] Mordike B, Ebert T. Magnesium: properties–applications–potential. Materials Science and Engineering:A. 2001; 302(1): 37-45.

[3] Witte F. The history of biodegradable magnesium implants: a review. Acta biomaterialia. 2010; 6(5):1680-1692.

[4] Payr E. Beitrge zur Technik der Blutgefss- und Nervennaht nebst Mitteilungen ber die Verwendung des resorbirbaren Metalles in der Chirurgie. Arch. Klin. Chir. 1900; 62:67-93.

[5] Walker J, Shandabaz S, Woodfield T, Staiger M, Dias G. Magnesium biomaterials for orthopedic application: A review from a biological perspective. Journal of Biomedical Materials Research B: Applied Biomaterials. 2014; 102(6):1316-1331.

[6] Staiger M, Pietak A, Huadmai J, Dias G. Magnesium and its alloys as orthopedic biomaterials: A review. Biomaterials.2006; 27(9):1728-1734.

[7] Bayraktar H, Morgan E, Niebur G, Morris G, Wong E, Keaveny T. Comparison of the elastic and yield properties of human femoral trabecular and cortical bone tissue. Journal of Biomechanics.2004; 37(1):27-35.

[8] Rack H, Qazi J. Titanium alloys for biomedical applications. Materials Science and Engineering:C.2006; 26(8):1269-1277.

[9] Horky J, Ghaffar A, Grill A, et al. Mechanical properties and microstructure of HPT-processed Mg-Zn-Ca alloys for biodegradable implants. In: Beausir B, Kasprzak N, Toth LS, editors. 6th international conference on nanomaterials by severe plastic deformation (NANOSPD6). Metz: University Press of Lorrain University; 2014.

[10] Valiev R, Estrin Y, Horita Z, Langdon T, Zehetbauer M, Zhu Y. Fundamentals of superior properties in bulk nanoSPD materials. Materials Research Letters.2015; 1-21.

[11] Kimura H, Maddin R. Quench hardening in metals. New York:American Elsevier Publishing Co Inc; 1971.

[12] Hull D, Bacon D. Introduction to dislocations Fourth Edition. Oxford:Butterworth-Heinemann;2001.

[13] Hampshire J , Hardie D. Hardening of pure magnesium by lattice defects. Acta Metallurgica.1974; 22(5):657-663.

[14] Kirchner HOK. Loop hardening of hexagonal metals. Zeitschrift fuer Metallkunde.1976; 67:525-532.

[15] Zehetbauer, M. Effects of non-equilibrium vacancies on strengthening. Key Engineering Materials.1995; 97:287-306.

[16] Zehetbauer M, Steiner G, Schafler E, Korznikov A, Korznikova E. Deformation induced vacancies with severe plastic deformation: Measurements and modelling. Materials Science Forum.2006; 503-504:57-64

[17] Wiederhorn S, Fields R, Low S, Bahng G-W, Wehrstedt A, Hahn J, Tomota Y, Miyata T, Lin H, Freeman B, et al. Mechanical properties. In: Czichos H, Saito T, Smith L, editors. Springer Handbook of Materials Measurement Methods. Berlin-Heidelberg:Springer-Verlag; 2006.

[18] Yoshinaga H, Horiuchi R. On the nonbasal slip in magnesium crystals. Transactions of the Japan Institute of Metals.1964; 5(1):14-21.

[19] Hutchinson W, Barnett M. Effective values of critical resolved shear stress for slip in polycrystalline magnesium and other hcp metals. Scripta materialia.2010; 63(7):737-740.

[20] Gottstein, G. Physikalische Grundlagen der Materialkunde.Berlin-Heidelberg:Springer-Verlag; 2007.

[21] Boehm, H. Einfhrung in die Metallkunde. [place unknown]:Bibliogr. Inst.; 1968.

[22] Gladman, T. Precipitation hardening in metals. Materials science and technology.1999; 15(1):30-36.

[23] Gladman, T. The physical metallurgy of microalloyed steels. London:The Institute of Materials;1997.

[24] Loeffler J, Uggowitzer P, Wegmann C, Becker M, inventors; BIOTRONIK SE & Co. KG, assignee. Process and apparatus for vacuum distillation of high-purity magnesium. EP 2804964 A1. 26. Nov. 2014.

[25] Shin D, Wolverton C. First-principles study of solutevacancy binding in magnesium. Acta Materialia.2010; 58(2):531-540.

[26] Hanawalt J, Nelson C, Peloubet J. Corrosion Studies of Magnesium and Its Alloys. trans. AIME.1942; 147:273-299.

[27] Mezbahul-Islam M, Mostafa A, Medraj M. Essential Magnesium Alloys Binary Phase Diagrams and Their Thermochemical Data. Journal of Materials.2014; 2014:1-32.

[28] Ghosh P, Mezbahul-Islam M, Medraj M. Critical assessment and thermodynamic modeling of Mg-Zn, Mg-Sn, Sn-Zn and Mg-Sn-Zn systems.Calphad.2012; 36:28-43.

[29] Spencer P, Pelton A, Kang Y, Chartrand P, Fuerst C. Thermodynamic assessment of the CaZn, SrZn, YZn and CeZn systems. Calphad.2008; 32(2):423-431.

[30] Aljarrah M, Medraj M. Thermodynamic modelling of the Mg-Ca, Mg-Sr,Ca-Sr and Mg-Ca-Sr systems using themodified quasichemical model. Calphad.2008; 32(2):240-251.

[31] Hofstetter J, Becker M, Martinelli E, Weinberg AM, Mingler B, Kilian H, Pogatscher S, Uggowitzer PJ, Loeffler JF. High-strength low-alloy (HSLA) MgZnCa alloys with excellent biodegradation performance. JOM.(2014; 66(4):566-572.

[32] Bamberger M, Levi G, Van der Sande J. Precipitation hardening in Mg-Ca-Zn alloys. Metallurgical and Materials Transactions A. 2006; 37(2):481-487.

[33] Zhilyaev A, Langdon T. Using high-pressure torsion for metal processing: Fundamentals and applications. Progress in Material Science.2008; 53:893-979.

[34] Valiev R, Estrin Y, Horita Z, Langdon T, Zehetbauer M, Zhu Y. Producing Bulk Ultrafine-Grained Materials by Severe Plastic Deformation.JOM.2006; 58(4):33-37.

[35] Thomas J, Gemming T. Analytical Transmission Electron Microscopy: An Introduction for Operators. Dordrecht: Springer Science + Business Media; 2014.

[36] Smith R, Sandland G. An Accurate Method of Determining the Hardness of Metals, with Particular Reference to Those of a High Degree of Hardness. Proceedings of the Institution of Mechanical Engineers. 1922; 102(1):623-64.

[37] Vickers hardness test [Internet]. [Updated 2016 Mar 8]. Wikimedia Foundation, Inc.; [cited 2016 Apr 13]. Available from:https://en.wikipedia.org/wiki/Vickers_hardness_test#cite_note-1

[38] [ISO] International Organization for Stardardization. Metallic MaterialsVickers Hardness Test. Part 1:Test Method.Geneva:ISO; (ISO standards handbooks: 3).2006.

[39] Brookes C, O'Neill J, Redfern B. Anisotropy in the hardness of single crystals. Proceedings of the Royal Society of London A: Mathematical, Physical and Engineering Sciences.1971; 322(1548):73-88.

[40] Shapiro S, Wilk M, Chen H. A comparative study of various tests for normality. Journal of the American Statistical Association.1968; 63(324):1343-1372.

[41] Histogram [Internet]. [Updated 2015].Wolfram.[cited 2016 Apr 13].Available from:http://reference.wolfram.com/language/ref/Histogram.html?q=Histogram

[42] Eckstein P. Angewandte Statistik mit SPSS. Wiesbaden:Gabler; 2000.

[43] Grnicher H. Messung beendet-was nun?: Einfhrung und Nachschlagewerk fr die Planung und Auswertung von Messungen. Zuerich:vdf Hochschulverlag AG; 1996.

[44] Mehta R. Interactions, Imaging and Spectra in SEM. INTECH Open Access Publisher; 2012.

[45] Suwas S, Ray R. Crystallographic texture of materials. London:Springer-Verlag; 2014.

[46] Goldstein J, Newbury D, Echlin P, Joy D, Romig A, Lyman C, Lifshin E. Scanning electron microscopy and X-ray microanalysis: a text for biologists, materials scientists, and geologists. New York:Plenum Press; 1992.

[47] Riedel E, Meyer H. Allgemeine und anorganische Chemie. Berlin:Walter de Gruyter; 2013.

[48] Craig B, Anderson D. Handbook of corrosion data. ASM international; 1994.

[49] Martienssen W. Semiconductors. In: Martienssen W, Warlimont H, editors. Springer Handbook of Condensed Matter and Materials Data. Berlin-Heidelberg:Springer-Verlag; 2006.

[50] Conrad H, Robertson WD. Effect of temperature on the flow stress and strain-hardening coefficient of magnesium single crystals. Transactions AIME.1957; 209:503-512.

[51] Heidenreich R, Matheson L. Electron microscopic determination of surface elevations and orientations. Journal of Applied Physics.1944; 15(5):423-435.

[52] Ashby M. Results and consequences of a recalculation of the Frank–Read and the Orowan stress. Acta Metallurgica.1966; 14(5):679-681.

[53] Xiaoxu H, Hansen N, Tsuji N. Hardening by annealing and softening by deformation in nanostructured metals.Science.2006; 312(5771):249-251.

[54] Renk O, Hohenwarter A, Schuh B, Li JH, Pippan R. Hardening by annealing: insights from different alloys. IOP Conference Series: Materials Science and Engineering. IOP Publishing.2015; 89(1):1-7

[55] Mathis K, Capek J, Zdrazilova Z, Trojanova Z.Investigation of tensioncompression asymmetry of magnesium by use of the acoustic emission technique.Materials Science and Engineering A.2011; 528:59045907.